Title: Type-I nNOS neurons orchestrate cortical neural activity and vasomotion

Authors: Kevin L. Turner[1,2,3.7], Dakota F. Brockway[4,7], Md Shakhawat Hossain[2,3,7], Keith R. Griffith[4,7], Denver I. Greenawalt[5,7], Qingguang Zhang[1,2,7,8], Kyle W. Gheres[1,2,7], Nicole A. Crowley[2,3,4,7], Patrick J. Drew[1,2,3,6,7]

Affiliations:

1. Department of Engineering Science and Mechanics, The Pennsylvania State University, University Park, PA 16802
2. Center for Neural Engineering, The Pennsylvania State University, University Park, PA 16802
3. Department of Biomedical Engineering, The Pennsylvania State University, University Park, PA 16802
4. Department of Biology, The Pennsylvania State University, University Park, PA 16802
5. Graduate Program in Molecular Cellular and Integrative Biosciences, The Pennsylvania State University, University Park, PA 16802
6. Department of Neurosurgery, The Pennsylvania State University, University Park, PA 16802
7. Penn State Neuroscience Institute, The Pennsylvania State University, University Park, PA 16802
8. Department of Physiology, Michigan State University, East Lansing, MI 48824

***Corresponding author:** Patrick J. Drew - pjd17@psu.edu

Acknowledgements: This work was supported by NIH Grants R01NS078168, R01NS079737, U19NS128613 to PJD, R01AA029403 to NAC, an American Heart Association Predoctoral fellowship 24PRE1201066 to MSH and F31ES036154 to DIG. DIG was supported by T32GM108563 and MSH was supported by T32NS115667.

Conflict of Interest: The authors declare no competing financial interests.

Author Contributions K.L.T, N.A.C, and P.J.D. designed the experiments. K.L.T, D.F.B, M.S.H, K.R.G, D.I.G, and Q.Z performed experiments. K.L.T., M.S.H, Q.Z, K.W.G., and P.J.D. analyzed the data. K.L.T. and P.J.D. wrote the paper.

Abstract: It is unknown how the brain orchestrates coordination of global neural and vascular dynamics. We sought to uncover the role of a sparse but unusual population of genetically distinct interneurons known as type-I nNOS neurons, using a novel pharmacological strategic to unilaterally ablate these neurons from the somatosensory cortex of mice. Region-specific ablation produced changes in both neural activity and vascular dynamics, decreased power in the delta-band of the local field potential, reduced sustained vascular responses to prolonged sensory stimulation, and abolished the post-stimulus undershoot in cerebral blood volume. Coherence between the left and right somatosensory cortex gamma-band power envelope and blood volume at ultra-low frequencies was decreased, suggesting type-1 nNOS neurons integrate long-range coordination of brain signals. Lastly, we observed decreases in the amplitude of resting-state blood volume oscillations and decreased vasomotion following the ablation of type-I nNOS neurons. This demonstrates that a small population of nNOS-positive neurons are indispensable for regulating both neural and vascular dynamics in the whole brain, raising the possibility that loss of these neurons could contribute to the development of neurodegenerative diseases and sleep disturbances.

Keywords: neurovascular coupling, type-I nNOS neurons, somatosensory cortex, two-photon, cerebral blood volume, widefield optical imaging, sleep

Introduction

Coordinated neural and hemodynamic activity across the brain are vital for arousal and cognition. The relationship between changes in neural activity and (typically measured) changes in blood volume, flow, and oxygenation, which are frequently studied with hemodynamic imaging and form the foundation of modern neuroscience, are mediated by local vasodilation and is known as neurovascular coupling (Drew 2019, Schaeffer & Iadecola 2021). Neurovascular coupling plays a critical role in supporting neuronal function, as tightly coordinated hemodynamic activity is essential for meeting energy metabolism and maintaining brain health (Iadecola et al 2023, Schaeffer & Iadecola 2021). The vasodilator nitric oxide (NO) (Hosford & Gourine 2019), produced by neuronal nitric oxide synthase (nNOS) in neurons, provides a key mechanism of arteriole dilation. Neurons in somatosensory cortex that express nNOS are activated by sensory stimulation, volitional whisking, and locomotion (Ahn et al 2023, Echagarruga et al 2020), all of which produce robust hemodynamic responses (Huo et al 2014, Winder et al 2017). Chemogenetic elevation or suppression of nNOS neuron activity alters both baseline diameter and behaviorally evoked dilation of arterioles (Echagarruga et al 2020). Similar vascular changes are produced by local infusion of a NOS inhibitor (Echagarruga et al 2020), implicating NO signaling directly in vascular regulation. Optogenetic activation of nNOS-positive neurons produces varying effects, with some reports demonstrating vasodilation and blood flow increases with minimal changes in neural activity (Krawchuk et al 2020, Lee et al 2020, Ruff et al 2024), while others show large, low-frequency EEG changes during sleep and quiet wakeful states (Gerashchenko et al 2018). While NO is known to modulate the excitability of neurons (Kara & Friedlander 1999, Smith & Otis 2003), artificial activation of nNOS neurons seems to drive vascular responses that are disproportionally larger than any corresponding neural changes, suggesting that this small population of neurons has an impact on vascular signals that is substantially greater than that of overall neural activity.

Two distinct GABAergic interneurons types express nNOS, denoted as type-I and type-II (Kawaguchi & Kubota 1997, Kubota et al 2011, Perrenoud et al 2012). nNOS-positive neurons make up approximately 20% of GABAergic interneurons in the cortex (Hendry et al 1987, Sahara et al 2012), with type-I constituting only 0.5–2% depending on brain region (Chong et al 2019, Tricoire & Vitalis 2012, Yan & Garey 1997). Type-I nNOS neurons are sparse, somatostatin-positive, most dense in the deep layers of cortex, and express nNOS at higher levels than type-II. They extend both local and long-range projections throughout the cortex, receive excitatory input from nearby pyramidal neurons and drive increases in cerebral blood flow when stimulated (Ruff et al 2024). Type-II nNOS neurons are in contrast much more abundant, smaller in size and morphology, and express nNOS less strongly than type-I. Type-II are a more heterogeneous group that express a variety of interneuron subtype markers and are more evenly distributed throughout the different layers of cortex (Perrenoud et al 2012, Yan et al 1996). Type-I nNOS neurons have been observed in rodents, carnivores, and primates (Higo et al 2007, Tomioka et al 2005, Tomioka & Rockland 2007) and are active during sleep (Dittrich et al 2015, Gerashchenko et al 2008, Kilduff et al 2011, Morairty et al 2013). In the cortex, type-I nNOS neuron density is anticorrelated with vascular density (Wu et al 2022). Type-I nNOS

neurons integrate local activity from feedforward excitatory pathways from the cortex and thalamus, likely contributing to the correlated changes in blood flow that are observed between functionally connected regions across hemispheres (Ruff et al 2024). Molecular, electrophysiological, and immunohistochemistry studies have demonstrated that type-I nNOS neurons are the only cells in the cortex that express the tachykinin receptor 1 (also known as neurokinin 1 receptor, TACR1/NK1R), the primary receptor for the endogenous neuropeptide substance P (Dittrich et al 2012, Endo et al 2016, He et al 2016, Huang et al 2016, Kubota et al 2011, Matsumura et al 2021, Paul et al 2017, Penny et al 1986, Ruff et al 2024, Vanlandewijck et al 2018, Vruwink et al 2001). Local infusion of substance P into the cortex causes a sustained increase in basal arterial diameter that is dependent upon local neural activity (Echagarruga et al 2020). Type-I nNOS neurons likely receive substance P from the ~40% of parvalbumin (PV)-positive cortical interneurons (Bugeon et al 2022, Pfeffer et al 2013, Vruwink et al 2001) that are thought to drive network synchrony (Cardin et al 2009, Sohal et al 2009). Optogenetic stimulation of PV neurons for several seconds drives a biphasic hemodynamic response, comprised of an early constriction (driven by suppression of overall population activity through GABA release), and a delayed, prolonged dilation lasting tens of seconds that is mediated indirectly by substance P (Vo et al 2023). The delayed vasodilation was not directly related to pyramidal neuron activity, was blocked by TACR1 antagonists, and was occluded by substance P, suggesting that activation of PV neurons drives downstream activation of type-I nNOS neurons. These experiments point to type-I nNOS neurons as having a large effect on vascular dynamics despite their smaller contribution in driving overall neural activity. However, optogenetic stimulation only activates one component of a circuit in isolation, in an otherwise healthy and intact microcircuit, potentially giving an incomplete picture of the neuron's role. Type-I nNOS neurons are uniquely vulnerable to stress (Han et al 2019), and their loss is likely in part causal to neurodegeneration (Iadecola et al 2023, Schaeffer & Iadecola 2021), making it vital to understand brain wide changes following a more physiologically-relevant model of perturbation.

Here we sought to reveal the role of type-I nNOS neurons in controlling neural and vascular dynamics in the cortex by selectively ablating them with saporin conjugated to a substance P analog (SP-saporin). Using this targeted ablation approach, we found that ablation of type-I nNOS neurons caused decreases in the hemodynamic response to sustained vibrissae stimulation, eliminated the post-stimulus undershoot, decreased local field potential power in the delta-band (1-4 Hz), reduced bilateral correlations in gamma-band power and blood volume across arousal states, and reduced the amplitude of resting-state blood volume oscillations. Together, these experiments demonstrate that a small subset of type-I nNOS neurons regulate key neural and vascular dynamics that coordinate changes in vasomotion.

Results

We investigated the effects of localized ablation of type-I nNOS neurons in somatosensory cortex on neurovascular coupling and functional connectivity in unanesthetized, head-fixed mice. C57BL6J mice (119 total, both male and female) were injected with either saporin conjugated to a substance P analog with high affinity for

104 the substance P receptor (SP-SAP) or a scrambled peptide as a control (Blank-SAP) into a localized region of one
105 hemisphere's somatosensory cortex. We used widefield optical imaging, electrophysiology, and 2-photon
106 microscopy to evaluate neural and hemodynamic changes following targeted ablation of type-I nNOS neurons in the
107 vibrissae (whisker) representation of somatosensory cortex while carefully monitoring arousal state (see **Materials**
108 **and Methods**). All imaging was performed during the animals' light cycle. Statistics included generalized linear
109 mixed-effects model (GLME), general linear models (GLM), or unpaired t-tests with corrections for multiple
110 comparisons when necessary.

111 **Saporin-conjugated peptides produce selective targeted ablation of type-I nNOS neurons**
112 While optogenetic and chemogenetic models give us insights into the potential function of neuron subtypes, it
113 is difficult to completely silence neurons in vivo, and the patterns of activity they induce are not physiological and
114 can have paradoxical effects on neural activity (Andrei et al 2021, Li et al 2019). Saporin provides a pharmacological
115 route to selectively kill only the cells that internalize it, and saporin conjugated to a peptide effectively targets
116 neurons that express a receptor for the peptide (Abbott et al 2012, McKay & Feldman 2008), allowing targeting of
117 specific cell types orthogonal to any genetic targeting techniques.

118 We first sought to validate the efficacy and specificity of saporin-based targeting of cortical TACR1-expressing
119 neurons. Type-I nNOS neurons were ablated by injection of the ribosome inactivating protein saporin (SAP),
120 conjugated either to substance P (SP-SAP) or a scrambled peptide as a control (Blank-SAP) (**Fig. 1a**). The SP-bound
121 SAP toxin binds to TACR1-expressing neurons (Martin & Sloviter 2001, Wang et al 2002, Wiley & Lappi 1999), which
122 in the cortex are exclusively expressed by type-I nNOS neurons (**Fig. 1b**). We used both immunofluorescence (**Fig.**
123 **1c**) and NADPH diaphorase staining (a histochemical marker for NOS, **Fig. S1**), to visualize nNOS neuron ablation
124 (Bredt et al 1991, Hope et al 1991, Hope & Vincent 1989). Immunofluorescent labeling in mice injected with Blank-
125 SAP showed labeling of nNOS-positive neurons near the injection site. In contrast, mice injected with SP-SAP showed
126 a clear loss in nNOS-labeling, with a typical spread of 1-2 mm from the injection site, though nNOS-positive neurons
127 both subcortically and in the entirety of the contralateral hemisphere remaining intact. We quantified the efficacy
128 of SP-SAP in removing type-I nNOS neurons by quantifying the number of nNOS-positive neurons per square mm of
129 cortical tissue (**Fig. 1d**), of which SP-SAP injected mice (N = 5, 3M/2F) had a significant reduction of nNOS-labeled
130 neurons (1.3 ± 1.6 neurons/mm^2) compared to Blank-SAP mice (N = 8, 4M/4F) with 10.3 ± 2.4 neurons/mm^2 (GLME
131 $p = 5.74\times10^{-6}$). It is unlikely that the disappearance of type-I nNOS neurons is because they stopped expressing nNOS,
132 as internalized saporin is cytotoxic. Exposure to SP-conjugated saporin causes rapid internalization of the SP
133 receptor-ligand complex (Mantyh et al 1995), and internalized saporin causes cell death via apoptosis (Bergamaschi
134 et al 1996). In the brain, the resulting cellular debris from saporin administration is then cleared by microglia
135 phagocytosis (Seeger et al 1997).

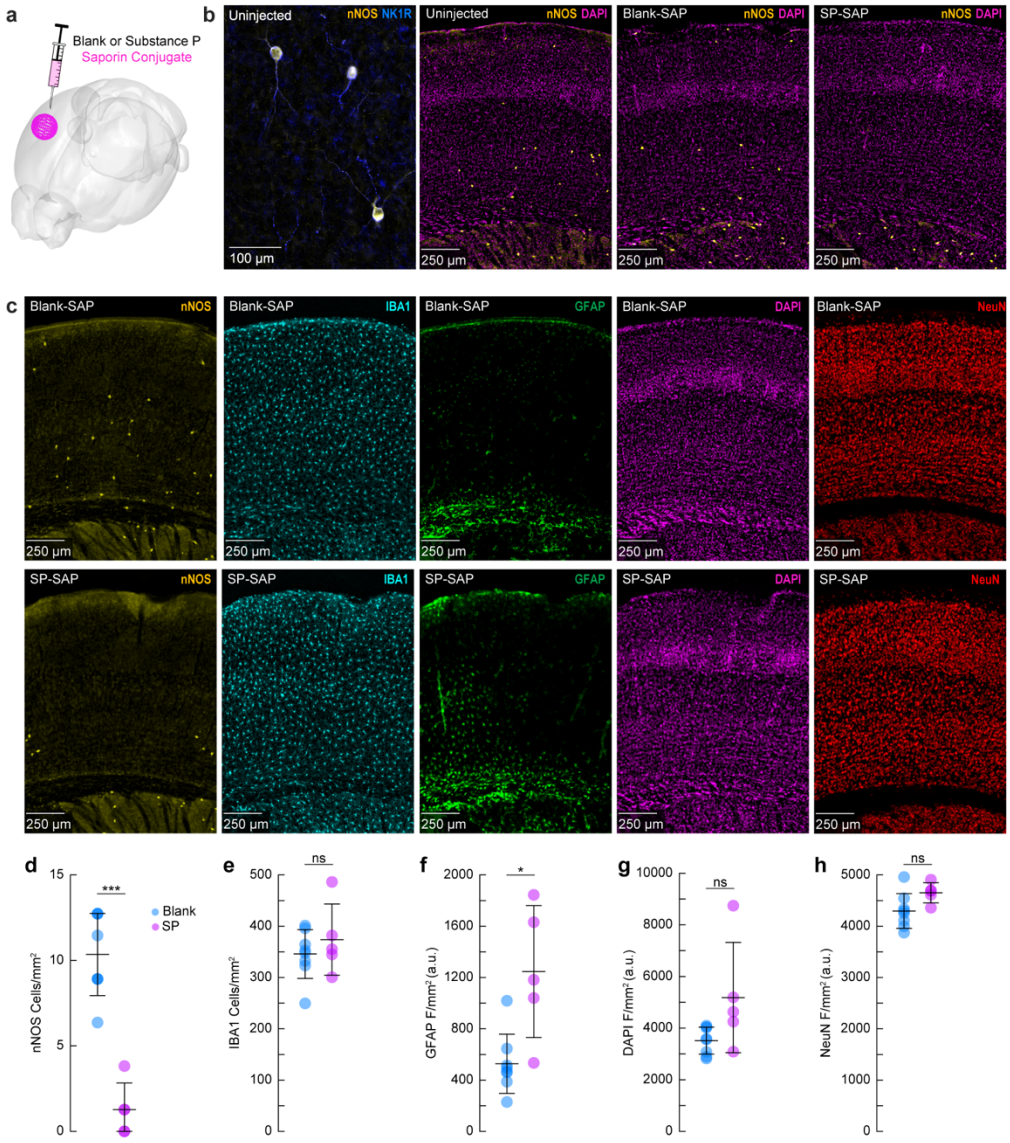

Figure 1. Saporin-conjugated peptides produce selective targeted ablation of type-I nNOS neurons (a) Schematic showing intracortical administration of the ribosome inactivating protein saporin conjugated to either SP or a vehicle control. **(b)** Representative immunofluorescence of anti-nNOS (yellow) and anti-NKR1 (blue) showing colocalization of the NK1 receptor on cortical nNOS-positive neurons. Representative immunofluorescence of anti-nNOS (yellow) and DAPI (magenta) from animals with no injection (Uninjected, left), Blank-SAP (middle), or SP-SAP (right). **(c)** Representative immunofluorescence of Blank-SAP (top) and SP-SAP (bottom) sections co-stained with nNOS (left), IBA1 (middle left), GFAP (middle), DAPI (middle right), or NeuN (right). NeuN image was taken from section immediately adjacent to the first four. **(d)** Quantification of nNOS counts, **(e)** IBA1 counts, **(f)** GFAP fluorescence, **(g)** DAPI fluorescence, **(h)** NeuN fluorescence. Error bars **(d-h)** denote SD. Bonferroni correction (5) *$\alpha < 0.01$, **$\alpha < 0.002$, ***$\alpha < 0.002$. **k-l** *$\alpha < 0.05$, **$\alpha < 0.01$, ***$\alpha < 0.001$, GLME.

We checked for non-specific effects driven by SP-SAP injections one-month post-administration by staining for ionized calcium binding adaptor molecule 1 (IBA1), glial fibrillary acidic protein (GFAP), DAPI, and NeuN (neuronal nuclei) as well as nNOS (as a positive control for ablation). There was no difference in the number of microglia (**Fig. 1e**) between groups (Blank-SAP: 345.8 ± 47.7 microglia/mm^2; SP-SAP: 373.8 ± 69.4 microglia/mm^2). There was an increase in GFAP labeling following SP-SAP injection (1246.3 ± 514.8 AU/mm^2; Blank-SAP: 527.2 ± 230.9 AU/mm^2, GLME p = 0.0029) (**Fig. 1f**). There was no significant difference in DAPI fluorescence (Blank-SAP: 3511.2 ± 524.42

142 AU/mm^2; SP-SAP: 5180.7 ± 2135.0 AU/mm^2; GLME p = 0.038, **Fig. 1g**) or NeuN fluorescence (Blank-SAP: 4296.8 ±
143 339.4 AU/mm^2; SP-SAP: 4652.1 ± 196.8 AU/mm^2; GLME p = 0.043, **Fig. 1h**) between groups after Bonferroni
144 correction for (5) multiple comparisons (**Fig. 1d-h**). Together, these findings indicate that the SP-SAP toxin was highly
145 selective in ablating type-I nNOS neurons with minimal non-specific effects. All mice that underwent imaging were
146 histologically verified for successful type-I nNOS neuron ablation using NADPH diaphorase staining. We quantified a
147 subset of these mice and saw a similar specific removal of type-I nNOS neurons (**Fig. S1)**. To determine if ablation of
148 type-I nNOS neurons from the somatosensory cortex had any impact on behavior or arousal state, we assayed
149 exploratory behavior, sleep, and pupil dynamics (**Fig. S2**). To assay exploratory behavior, mice were placed in a novel
150 open field environment and allowed to explore for 5 minutes while quantifying distance traveled and time spent in
151 the center, two metrics for evaluating stress and anxiety in rodents (Roth & Katz 1979, Seibenhener & Wooten 2015).
152 We noted no differences in any metric evaluating open field behavior (N = 12-23 mice/group). We also assessed
153 multiple measurements of sleep quality and quantity. There was no difference in the percentage of time each mouse
154 spent in rapid eye movement (REM) or non-REM (NREM) sleep, or the percentage of time they spent volitionally
155 whisking while awake (N = 9 mice/group). We also noted no significant differences in eye-related arousal state
156 metrics including interblink-interval, pupil size, and pupillary response to vibrissae stimulation (Turner et al 2023).
157 Together, this suggests that ablation of type-I nNOS neurons had no gross effects on sleep or general ambulatory
158 behavior.

159 **Impact of type-I nNOS neuron removal on neural and hemodynamic signals across arousal states**

160 To determine the impact localized ablation of type-I nNOS neurons had on neural and hemodynamic signals in
161 the somatosensory cortex, we used widefield optical imaging (Huo et al 2014, Sirotin & Das 2009) to measure
162 changes in total hemoglobin (Δ[HbT], an indicator of blood volume). We measured neural activity using either
163 implanted electrodes (Winder et al 2017) to measure changes in local field potential (LFP) (**Fig. 2a, c, d**), or in a
164 separate cohort of mice, pan-neuronal expression of the calcium indicator GCaMP7s (Chan et al 2017, Dana et al
165 2019), which provides complementary measures of bulk neural activity (**Fig. 2b, e, f**). In mice expressing GCaMP7s,
166 we measured Δ[HbT], as well as changes in cerebral oxygenation (Δ[HbO]) and deoxygenation (Δ[HbR]) using
167 alternating illumination at 480/530/630 nm (Ma et al 2016a, Ma et al 2016b, Zhang et al 2019). We corrected for
168 hemodynamic contamination of GCaMP7s signals using the simultaneously acquired hemoglobin signals (Kramer &
169 Pearlstein 1979, Ma et al 2016a, Scott et al 2018, Wright et al 2017). Measurements of neural and hemodynamic
170 signals were taken bilaterally through polished and reinforced thinned-skull windows (Drew et al 2010, Shih et al
171 2012) in the vibrissae representation of somatosensory cortex. Each animal was habituated to head-fixation over
172 the course of several days following surgery. For the first 60 minutes of each recording session, the vibrissae were
173 briefly stimulated with directed puffs of air to either the left or right pad, or by a puffer directed away from the

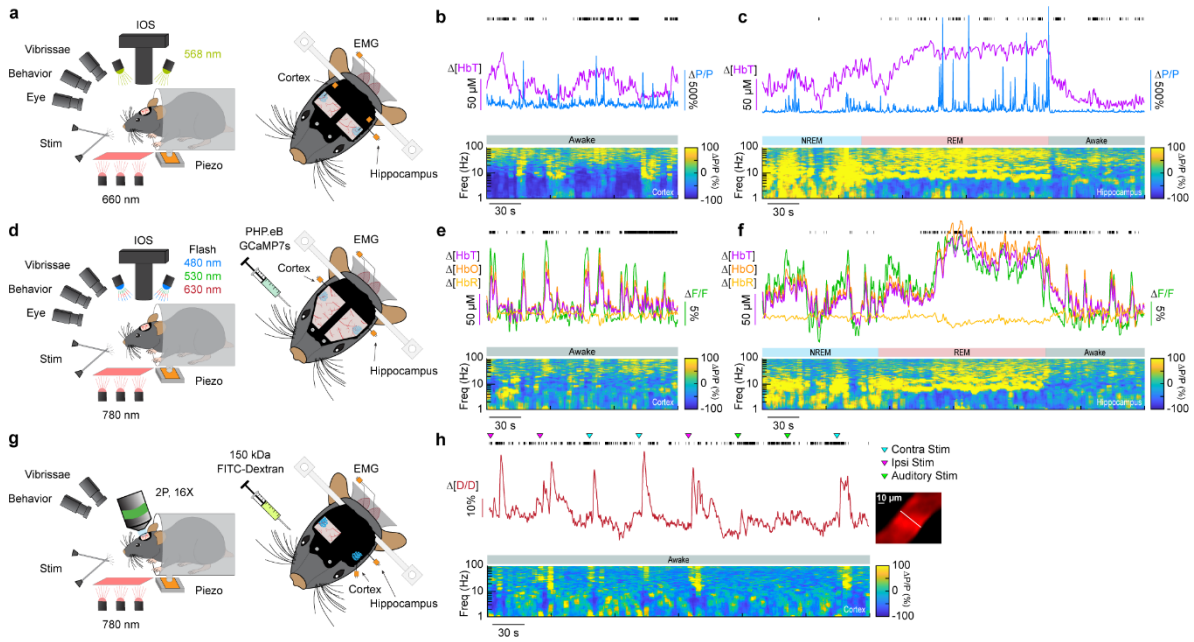

Figure 2. Impact of type-I nNOS neuron removal on neural and hemodynamic signals across arousal states (a) Schematic of widefield optical imaging experimental setup. The brain is illuminated at an isosbestic wavelength of hemoglobin (568 nm). Changes in reflected light measuring changes in total blood volume are captured by a camera mounted above the head while several other cameras monitor animal behavior and arousal state including vibrissae and pupil tracking. Vibrissae stimulation is done by directed air puffs. Polished and reinforced thinned-skull windows were bilaterally implanted over the somatosensory cortex. Tungsten stereotrodes were implanted underneath each window to record changes in local field potential within the area of interest (relative change in power, ΔP/P). An additional hippocampal stereotrode and a neck electromyography electrode were used to assist in sleep scoring. **(b,e,h)** During the awake state, power in low-frequency cortical LFP is low and power in the gamma-band (30-100 Hz) is elevated during activity such as volitional whisking. **(c, f)** Periods of NREM and REM sleep are accompanied by large oscillations in cerebral blood volume, with large increases in power in delta-band (1-4 Hz) cortical LFP during NREM and large increases in theta-band (4-10 Hz) hippocampal LFP during REM. Black tick marks indicate vibrissae motion. **(d)** Schematic of widefield optical imaging experiments with GCaMP7s. Alternating illumination with 480 nm, 530 nm, and 630 nm light were used to measure changes in total hemoglobin, blood oxygenation, and GCaMP7s fluorescence. (g) Schematic of two photon experiments.

mouse as an auditory control (Drew et al 2011). Afterwards, each mouse was given several hours to naturally sleep with no stimulation. To determine the arousal state of the mouse, we performed electromyography of the nuchal muscles of the neck, tracked vibrissae movement and pupil diameter using video, and body movements with a force sensor. Arousal state was scored in 5 second intervals as either Awake, NREM, or REM as previously described (Turner et al 2020) from behavioral and physiological data using a bootstrapped random forest classification algorithm. We saw no differences in the accuracy or validity of our sleep-scoring models across different experimental conditions (Blank-SAP; SP-SAP; Uninjected) (**Fig. S3**).

Ablation of type-I nNOS neurons reduces the stimulus-evoked response

We first determined the impact of removal of type-I nNOS neurons on evoked hemodynamic signals. The initial increase in blood volume in response to brief (0.1 second) stimulation of the contralateral vibrissae was not affected by ablation of type-I nNOS neurons (**Fig. 3a**), but the post-stimulus undershoot was absent in the SP-SAP mice. When we evaluated the canonical post-stimulus hemodynamic undershoot from 2:4 seconds, the Blank-SAP group (N = 9, 5M/4F) had a mean of -2.2 ± 0.5 μM, compared to the SP-SAP group (N = 9, 5M/4F) mean of 1.0 ± 0.6 μM (GLME *p*

= 0.0005). This result is consistent with the observation that type-I nNOS neurons express the vasoconstrictory

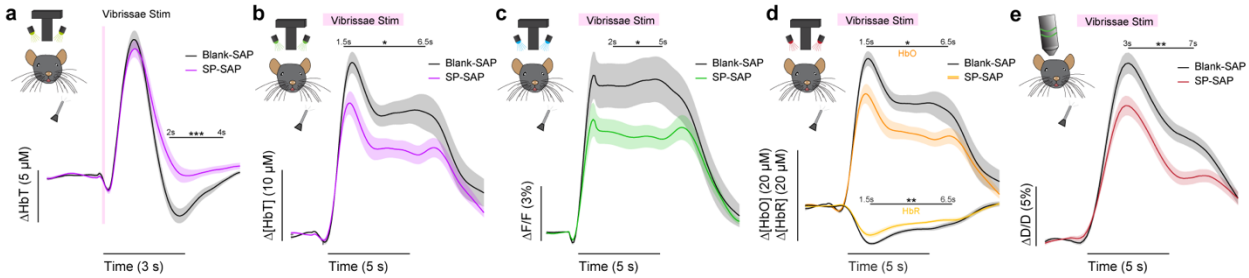

Figure 3. Ablation of type-I nNOS neurons reduces the stimulus-evoked response (a) Change in total hemoglobin in response to brief (0.1 second) vibrissae stimulation. **(b)** Change in total hemoglobin in response to extended (5 seconds) vibrissae stimulation. **(c)** Change in GCaMP fluorescence in response to extended vibrissae stimulation. **(d)** Change in oxy- and deoxy- hemoglobin in response to extended vibrissae stimulation. **(e)** Change in arteriole diameter in response to extended vibrissae stimulation. Error bars represent population averages ± SEM. All statistics were evaluated between the indicated intervals. *p < 0.05, **p < 0.01, ***p < 0.001, GLME.

neuropeptide Y (NPY) (Karagiannis et al 2009) which is thought to underlie this post-stimulus undershoot (Uhlirova et al 2016). It is also possible that loss of NO signaling from type-I nNOS neurons could also contribute through interactions with blood volume to generate oscillations and post-dilation undershoots (Haselden et al 2020). Using three-wavelength spectroscopy in mice expressing GCaMP7s, we saw consistent increases in blood volume, neural activity, and cerebral oxygenation during prolonged (5 seconds) vibrissae stimulation. Δ[HbT] evaluated 1.5:6.5 seconds following stimulus-onset decreased from 18.7 ± 1.7 μM in Blank-SAP (N = 7, 3M/4F) to 13.1 ± 1.4 μM in SP-SAP (N = 8, 4M/4F, GLME p = 0.017) (**Fig. 3b**). Calcium signals (**Fig. 3c**) evaluated 2:5 seconds following stimulus onset decreased from 8.2 ± 1.3 % in Blank-SAP to 5.3 ± 0.7 % in SP-SAP (GLME p = 0.047). Δ[HbO] (**Fig. 3d**) evaluated 1.5:6.5 seconds following stimulus onset decreased from 24.6 ± 1.9 μM in Blank-SAP to 17.4 ± 1.7 μM in SP-SAP (GLME p = 0.010) while Δ[HbR] evaluated from 1.5:6.5 seconds increased from -6.0 ± 0.4 in Blank-SAP to -4.4 ± 0.3 in SP-SAP (GLME p = 0.005). Evaluation windows were determined based on the duration of stimuli and the delayed onset of the hemodynamic response.

We further investigated single arterial dynamics during vibrissae stimulation with 2-photon microscopy. Following ablation of type-I nNOS neurons, after vibrissae stimulation there was a decrease in arteriole diameter (**Fig. 3e**) evaluated 3:7 seconds following stimulus onset from 11.6 ± 0.8 %·s in Blank-SAP (N = 9, 5M/4F, n = 81 arterioles) down to 7.8 ± 0.6 % in SP-SAP (N = 7, 2M/5F, n = 70 arterioles, GLME p = 0.008). The arterial changes closely mirror the Δ[HbT] changes, consistent with the substantial contribution of arterial dynamics to the blood volume signal (Huo et al 2015). We also evaluated changes in blood volume during voluntary locomotion, where we saw a similar trend in decrease in locomotion-evoked Δ[HbT] evaluated 1.5:2.5 seconds following locomotion onset from 17.5 ± 2.0 μM in Blank-SAP (N = 7, 5M/2F) to 12.9 ± 2.0 μM in SP-SAP (N = 7, 2M/5F), but it was not statistically significant (GLME p = 0.10). These results show the removal of a very small number of neurons can drive substantial reductions in both hemodynamic and neural response to sensory stimulation.

Type-I nNOS ablation reduces low frequency neural activity and gamma-band neurovascular coupling

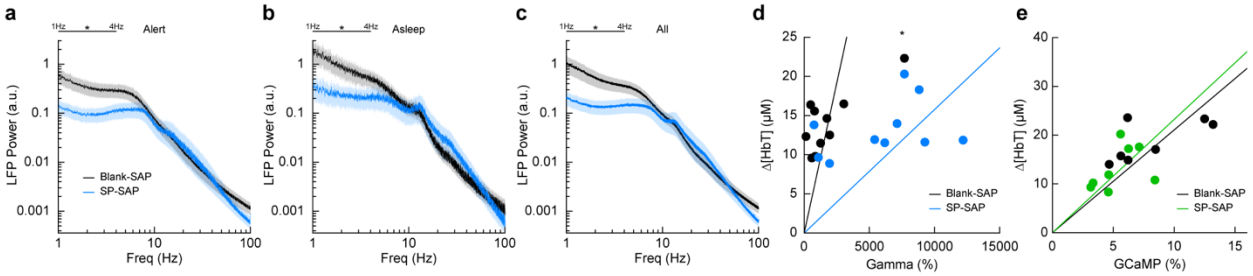

Figure 4. Type-I nNOS ablation alters low frequency neural activity and gamma-band neurovascular coupling (a) Local field potential within the vibrissae representation of somatosensory cortex during periods of Alert. **(b)** Asleep. **(c)** All data. **(d)** Change in gamma-band power vs. Δ[HbT] following brief (0.1 seconds) vibrissae stimulation. **(e)** Change in GCaMP7s fluorescence vs. Δ[HbT] following prolonged (5 seconds) vibrissae stimulation. Error bars represent population averages ± SEM. All statistics were evaluated between the indicated intervals. *p < 0.05, **p < 0.01, ***p < 0.001, GLME (**a-c**), GLM (**d, e**).

To determine the effect that type-I nNOS neuron removal had on neural activity, we assessed the power spectrum of the LFP in different arousal states, which we classified into alert, asleep, and all data (Turner et al 2020). Data was classified into the alert state when 15-minute blocks were predominantly (> 80%) in the awake state. Alert periods contained fidgeting movements and bouts of whisking interspersed with awake quiescence. Periods classified as asleep were predominantly composed of sleeping states (NREM/REM > 80% of all classifications in a 15-minute block) with only brief periods of wakefulness, typically occurring during transitions between sleep states. The 'all' state includes everything irrespective of arousal state classification. The first ~60 minutes of each recording session which included vibrissae stimulation was excluded. There was a pronounced reduction in the delta-band (1-4 Hz) power of the LFP in all three arousal state categories. The power in the delta-band of the LFP in Blank-SAP mice (N = 9, 4M/5F) in the alert state (**Fig. 4a**) was $3.4\times10^{-10} \pm 1.0\times10^{-10}$ a.u. compared to $1.0\times10^{-10} \pm 3.0\times10^{-11}$ a.u. in the SP-SAP mice (N = 9, 5M/4F, GLME $p = 0.011$). The power in the delta-band of the LFP in Blank-SAP mice (N = 7, 3M/4F) in the asleep state (**Fig. 4b**) was (NREM + REM) was $8.5\times10^{-10} \pm 3.0\times10^{-10}$ a.u. compared to $2.4\times10^{-10} \pm 9.1\times10^{-11}$ a.u. in the SP-SAP mice (N = 7, 4M/3F, GLME $p = 0.022$). The power in the delta-band of the LFP in Blank-SAP mice (N = 9, 4M/5F) averaged across all arousal states (**Fig. 4c**) was $5.2\times10^{-10} \pm 1.7\times10^{-10}$ a.u. compared to $1.5\times10^{-10} \pm 4.3\times10^{-11}$ a. u. in the SP-SAP mice (N = 9, 5M/4F, GLME $p = 0.016$). These result parallel those seen in studies where knockout of nNOS produces lower delta band power (Morairty et al 2013) and optogenetic stimulation of nNOS neurons produces low frequency oscillations (Zielinski et al 2019), suggesting that type-I nNOS neurons promote these slow oscillations via NO release. In contrast to the observed reductions in LFP in the ablated hemisphere, we noted no gross changes in the power spectra of neural LFP in the unablated hemisphere **(Fig. S7)** or power of the cerebral blood volume fluctuations in either hemisphere (**Fig. S4)**.

We next wanted to see whether the amount of neural activity and corresponding Δ[HbT] in response to vibrissae stimulation was altered following type-I nNOS neuron ablation. As a measure of neurovascular coupling, we used the slope of the line fitting the change in gamma-band power vs. Δ[HbT] following brief (0.1 second) vibrissae stimulation (**Fig. 4d**). Decreases in the slope indicate a smaller vascular response for a given amount of neural

activity, indicating a decrease in neurovascular coupling. We found the slope was significantly increased in SP-SAP mice compared to Blank-SAP mice (Blank-SAP: 0.02 ± 0.03; SP: 0.005 ± 0.006, GLM p = 0.0001). We also evaluated the change in GCaMP7s fluorescence vs. Δ[HbT] during prolonged (5 seconds) vibrissae stimulation from 2:5 seconds (**Fig. 4e**) and saw no significant change in the slope (Blank-SAP: 251.3 ± 75.3; SP: 256.5 ± 73.2, GLM p = 0.34). Given that the sensory-evoked LFP is driven more by synaptic input, while GCaMP7s signals are driven by local neural activity, these results indicate that the loss of type-I nNOS neurons reduces overall excitability, but that the input drive from other areas might be increased, potentially due to homeostatic mechanisms at the input synapses (Turrigiano 2008).

Neurovascular coupling was weakly affected by type-I nNOS removal

We next looked at the cross-correlation between blood volume and neural signals, which provides a measure of spontaneous neurovascular coupling. For electrophysiological measures, we measured the cross-correlation between gamma-band power and blood volume (**Fig. 5a**). We evaluated the peak cross-correlation during the resting-state, during long periods while alert, or long periods while asleep. The cross-correlation between neural activity and hemodynamic signals is substantially higher during periods of behavior (whisking, fidgeting) than during the resting-state because self-generated motion and whisking drive increases in neural activity and vasodilation (Claron et al 2023, Drew et al 2019, Stringer et al 2019, Tu et al 2024, Winder et al 2017) . The correlation between neural activity and blood volume changes is higher during sleep than in the awake state (Turner et al 2020). We saw no significant difference in the peak cross-correlation during the resting-state (**Fig. 5b**) between Blank-SAP mice (N = 9, 4M/5F, 0.08 ± 0.007) and SP-SAP mice (N = 9, 5M/4F, 0.06 ± 0.008, GLME p = 0.22). We did observe a significant difference in the peak cross-correlation during both periods of alert and asleep, from 0.23 ± 0.01 (Blank-SAP) to 0.16 ± 0.03 (SP-SAP, GLME p = 0.036) during alert periods (**Fig. 5c**) and 0.40 ± 0.02 (Blank-SAP) dropping to 0.33 ± 0.02 (SP-SAP, GLME p = 0.012) while asleep (**Fig. 5d**). We next wanted to evaluate whether this drop in neurovascular coupling was more prevalent at a particular modulation frequency. When analyzing the coherence between the gamma-band power and hemodynamic signals during these different arousal states, we noted no dominant frequency and saw no significant changes in the lower frequencies associated with neurovascular coupling (≤ 0.5 Hz). During the resting-state (**Fig. 5e**), the average coherence between 0.1 and 0.5 Hz was 0.28 ± 0.008 in Blank-SAP mice and 0.23 ± 0.01 in SP-SAP mice (GLME p = 0.23). The average coherence between 0.01 and 0.5 Hz during alert periods (**Fig. 5f**) was 0.29 ± 0.004 in Blank-SAP mice and 0.25 ± 0.005 in SP-SAP mice (GLME p = 0.06), and during asleep periods (**Fig. 5g**) it was 0.34 ± 0.008 in Blank-SAP mice and 0.32 ± 0.007 in SP-SAP mice (GLME p = 0.46). Lastly, to evaluate any changes in the predictive power of the neural-hemodynamic relationship, we fit a hemodynamic response function using the gamma-band power and hemodynamic response following periods of vibrissae stimulation. We observed that ablation of Type-I nNOS neurons did not alter the predictive power of the hemodynamic response function (**Fig. S5**).

We next evaluated neurovascular coupling from optical measures of bulk activity using GCaMP7s (**Fig. 5h**). The peak resting-state cross-correlation (**Fig. 5i**) between GCaMP7s fluorescence and ongoing hemodynamics showed a significant decrease, 0.68 ± 0.02 with Blank-SAP versus 0.62 ± 0.02 with SP-SAP (GLME p = 0.038). However, there was no drop in peak cross-correlation during either alert or asleep as seen with the gamma-band power. During alert periods (**Fig. 5j**), the peak GCaMP7s cross-correlation was 0.78 ± 0.12 with Blank-SAP and 0.77 ± 0.02 with SP-SAP (GLME p = 0.54) while during asleep periods (**Fig. 5k**) it was 0.88 ± 0.008 with Blank-SAP and 0.86 ± 0.04 with SP-SAP (GLME p = 0.58). Like the peak in cross-correlation, the average resting-state coherence (**Fig. 5l**) did show a significant drop across the lower frequencies, 0.75 ± 0.01 with Blank-SAP vs. 0.70 ± 0.01 with SP-SAP (GLME p = 0.049). There was no drop in coherence during alert periods (**Fig. 5m**) at 0.78 ± 0.005 with Blank-SAP and 0.77 ± 0.004 with SP-SAP (GLME p = 0.42) nor during asleep periods (**Fig. 5n**) at 0.75 ± 0.009 with Blank-SAP and 0.74 ± 0.01 with SP-SAP (GLME p = 0.63). While there are small changes in neural-hemodynamic correlations, the differences in neurovascular coupling across arousal states were relatively small following localized removal of type-I nNOS neurons, meaning any effects of ablation on hemodynamic responses are primarily mediated by changes in neural activity.

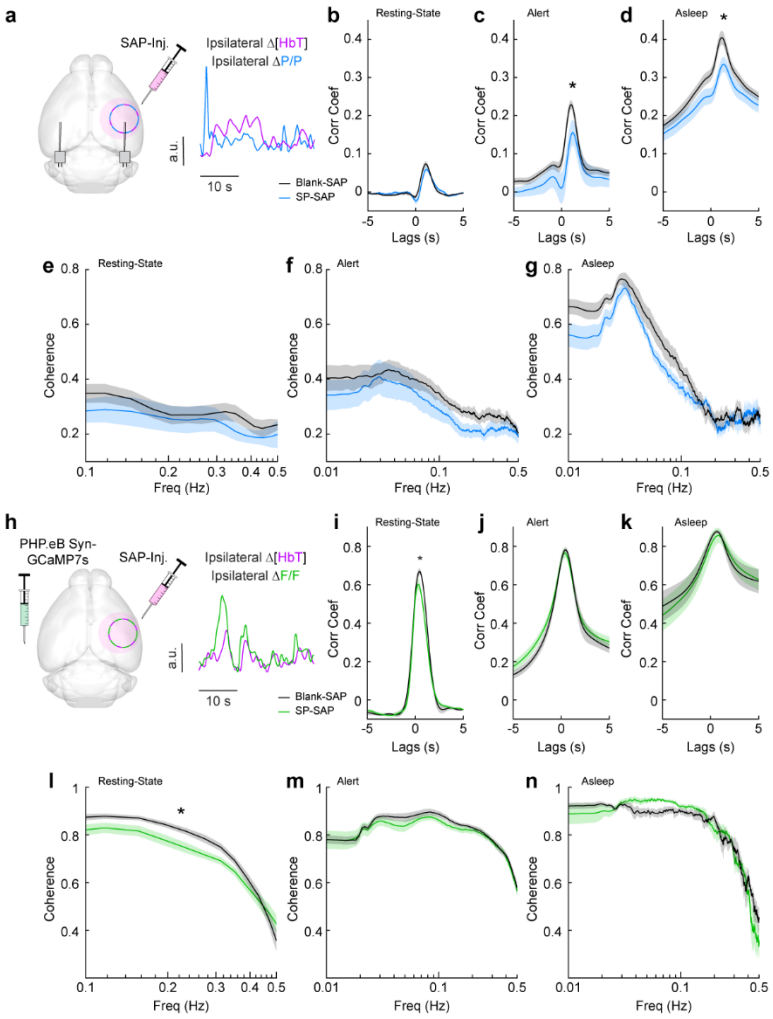

Figure 5. Neurovascular coupling was only weakly affected by type-I nNOS removal (a) Schematic demonstrating intracortical injection of either Blank-SAP or SP-SAP and the analysis of gamma-band power and hemodynamic signals from within the vibrissae representation of somatosensory cortex, N = 9 mice per group. **(b)** Gamma-Δ[HbT] resting-state cross-correlation **(c)** Gamma-Δ[HbT] alert cross-correlation **(d)** Gamma-Δ[HbT] asleep cross-correlation **(e)** Gamma-Δ[HbT] resting-state coherence **(f)** Gamma-Δ[HbT] alert coherence **(g)** Gamma-Δ[HbT] asleep coherence **(h)** Schematic demonstrating intracortical injection of either Blank-SAP or SP-SAP and the analysis of GCaMP7s fluorescence and hemodynamic signals from within the vibrissae cortex, n = 6-7 mice per group. **(i)** GCaMP7s-Δ[HbT] resting-state cross-correlation **(j)** GCaMP7s-Δ[HbT] alert cross-correlation (k) GCaMP7s-Δ[HbT] asleep cross-correlation **(l)** GCaMP7s-Δ[HbT] resting-state coherence **(m)** GCaMP7s-Δ[HbT] alert cross-correlation **(n)** GCaMP7s-Δ[HbT] asleep cross-correlation. Error bars represent population averages ± SEM. *p < 0.05, **p < 0.01, ***p < 0.001, GLME.

Type-I nNOS ablation reduces low-frequency interhemispheric coherence

Because type-I nNOS neurons send and receive many modulatory signals across a range of distances, they could help serve to coordinate neural and vascular dynamics across the brain. We tested this hypothesis by comparing how loss of type-I nNOS neurons changed the coherences of neural and hemodynamics signals between the left and right vibrissae cortex, which are generally highly correlated across all behaviors and frequencies (Turner et al 2020). Neural activity is also bilaterally correlated, though less so than vascular dynamics. Average resting-state coherence between the left and right Δ[HbT] signals (**Fig. 6a**) in the vibrissae cortex were 0.79 ± 0.005 for Blank-SAP and 0.73 ± 0.008 for SP-SAP mice (p = 0.014, GLME, **Fig. 6b**). This reduction in coherence was seen over all frequencies (0-0.5 Hz) during both alert periods (**Fig. 6c**), at 0.86 ± 0.002 for Blank-SAP and 0.81 ± 0.003 for SP-SAP ($p = 7.4\times10^{-6}$, GLME), as well as asleep periods (**Fig. 6d**) with 0.86 ± 0.003 for Blank-SAP and 0.79 ± 0.005 for SP-SAP (p = 0.0008, GLME).

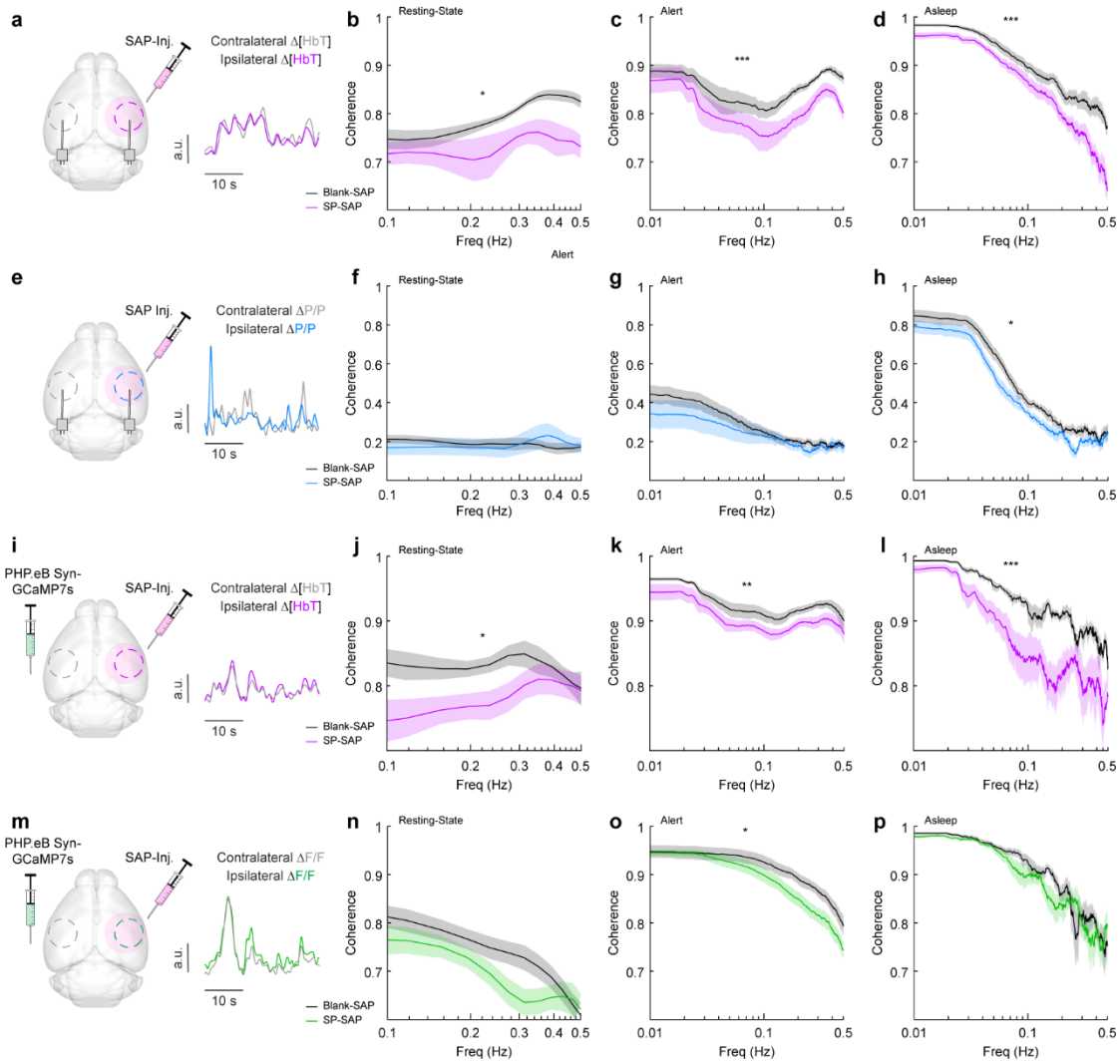

Figure 6. Type-I nNOS ablation reduces low-frequency interhemispheric coherence (a) Δ[HbT] coherence between bilateral ROIs in the left and right hemisphere's somatosensory cortex during **(b)** Res.t **(c)** Alert. **(d)** Asleep. **(e)** Gamma-band power coherence between bilateral ROIs in the left and right hemisphere's somatosensory cortex during **(f)** Res.t **(g)** Alert. **(h)** Asleep. **(i)** Δ[HbT] coherence between bilateral ROIs in the left and right hemisphere's somatosensory cortex during **(j)** Res.t **(k)** Alert. **(l)** Asleep. **(m)** GCaMP7s coherence between bilateral ROIs in the left and right hemisphere's somatosensory cortex during **(n)** Res.t **(o)** Alert. **(p)** Asleep. Error bars represent population averages ± SEM. *p < 0.05, **p < 0.01, ***p < 0.001, GLME.

We then looked at the coherence of gamma-band power across hemispheres, where average coherence for bilateral gamma-band signals in the resting-state were 0.19 ± 0.006 (Blank-SAP) and 0.19 ± 0.01 (SP-SAP, p = 0.88, GLME, **Fig 6e, f**). There was no significant difference during the alert periods (**Fig 6g**) at 0.22 ± 0.005 (Blank-SAP) and 0.20 ± 0.006 (SP-SAP, p = 0.43, GLME), but ablation of type-I nNOS neuros produced a reduction of coherence during asleep periods (**Fig. 6h**) at 0.35 ± 0.009 (Blank-SAP) and 0.29 ± 0.009 (SP-SAP, p = 0.047, GLME).

Average resting-state coherence across bilateral Δ[HbT] signals (**Fig. 6i**) taken from the vibrissae cortex were 0.83 ± 0.005 (Blank-SAP) and 0.78 ± 0.007 (SP-SAP, p = 0.021, GLME, **Fig. 6j**). This reduction in coherence persisted across all frequencies during the both alert periods (**Fig. 6k**) at 0.92 ± 0.001 (Blank-SAP) and 0.90 ± 0.001 (SP-SAP, p = 0.012, GLME) as well as sleep periods (**Fig. 6l**) at 0.90 ± 0.002 (Blank-SAP) and 0.83 ± 0.005 (SP-SAP, p = 0.004, GLME). Average resting-state coherence across bilateral GCaMP7s signals (**Fig. 6m**) taken from the vibrissae cortex were 0.75 ± 0.009 (Blank-SAP) and 0.70 ± 0.009 (SP-SAP, GLME p = 0.12, **Fig. 6n**). This reduction in coherence persisted across all frequencies during the both alert periods (**Fig. 6o**) at 0.88 ± 0.003 (Blank-SAP) and 0.84 ± 0.003 (SP-SAP, p = 0.029, GLME) but not in sleep periods (**Fig. 6p**) at 0.85 ± 0.005 (Blank-SAP) and 0.84 ± 0.005 (SP-SAP, GLME p = 0.52). When the correlation of bilateral signals was evaluated with Pearson's correlation coefficients, the same general trend remained (**Fig. S6**). These results show that removal of type-I nNOS neurons reduces both vascular and neural coordination across hemispheres. This loss of coherence does not imply that removal of type-I nNOS neurons has direct effects on the contralateral hemisphere, just that the dynamics in the ablated hemisphere have been altered so they no longer respond effectively to input from the ipsilateral hemisphere and/or common sources of modulatory drive that act through type 1 nNOS neurons (e.g. hypocretin (Williams et al 2019), or cholinergic inputs (Williams et al 2018)).

Type-I nNOS neurons control vasomotion power but not baseline diameter

We next wanted to establish how ablation of type-I nNOS neurons affected vasomotion, spontaneous oscillations in the absence of behavior, measured at the scale of blood volume and at the level of single arterioles, as well as the basal tone of blood vessels. The variance in Δ[HbT] during rest, a measure of vasomotion amplitude, was significantly reduced following type-I nNOS ablation (**Fig. 7a**), dropping from 40.9 ± 3.4 μM^2 in the Blank-SAP

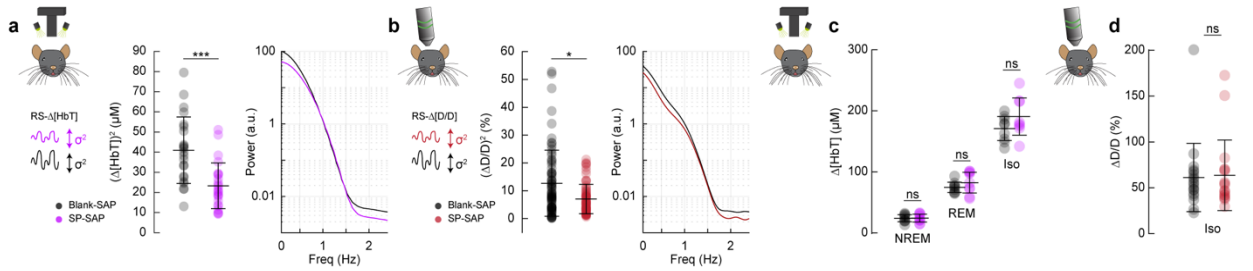

Figure 7. Type-I nNOS neurons control vasomotion power but not baseline diameter (a) Variance (proportional to average power) in the resting-state hemodynamics signals measured with widefield optical imaging. **(b)** Variance in resting-state arteriole diameter measured with two-photon. **(c)** Average Δ[HbT] during periods of NREM sleep, periods of REM sleep, and following administration of isoflurane (n = 9 mice per group). **(d)** Change in normalized arteriole diameter following administration of isoflurane. Error bars represent population averages ± SD. All statistics were evaluated between the indicated intervals. *p < 0.05, **p < 0.01, ***p < 0.001 GLME.

group (N = 24, 12M/12F) to 23.3 ± 2.3 μM^2 in the SP-SAP group (N = 24, 11M/13F) (GLME $p = 6.9\times10^{-5}$) with no significant difference in the unablated hemisphere (Fig. S7). Individual pial and penetrating arterioles showed the same reduction in vasomotion after type-I nNOS neuron ablation, with Blank-SAP (N = 9, 5M/4F, n = 70 arterioles) having a resting diameter variance of 12.6 ± 1.4 $\%^2$ and SP-SAP (N = 7, 2M/5F, n = 65 arterioles) of 8.0 ± 0.8 $\%^2$ (**Fig. 7b**). There was no difference in resting-state (baseline) diameter between the groups, with Blank-SAP having a diameter of 24.4 ± 7.5 µm and SP-SAP having a diameter of 23.0 ± 9.4 µm (ttest, p = 0.61).

If type-I nNOS neurons control the basal diameter of vessels via secreted vasodilators, potentially in an arousal state dependent way, when we ablate these neurons we would observe a difference in blood volume across arousal states and in the maximal dilation elicited with isoflurane (Gao et al 2015). We saw no changes in the average change in Δ[HbT] across states (**Fig. 7c**, **Fig. S8**). The resting-state Δ[HbT] in Blank-SAP mice was 0.29 ± 0.7 µM compared to 0.29 ± 0.9 µM in SP-SAP (GLME $p = 0.997$). NREM Δ[HbT] in Blank-SAP mice was 23.9 ± 5.8 µM compared to 24.1 ± 6.5 µM in SP-SAP (GLME $p = 0.96$). REM Δ[HbT] in Blank-SAP mice was 74.5 ± 8.4 µM compared to 82.3 ± 17 µM in SP-SAP (GLME $p = 0.26$). The Δ[HbT] following isoflurane in Blank-SAP mice was 170.9 ± 19.7 µM compared to 190.5 ± 30.5 µM in SP-SAP (GLME $p = 0.15$). We repeated the isoflurane experiment on a set of pial and penetrating arterioles under 2-photon microscopy. The change in normalized arteriole diameter following administration of isoflurane (n = 7-9 mice per group, 18-19 arterioles per group) was 61.2 ± 37.2% in Blank-SAP (baseline diameter 23.2 ± 6.6 µm) compared with 63.6 ± 38.4% in SP-SAP (baseline diameter 23.0 ± 10.2 µm, $p = 0.85$, ttest). These results indicate that type-I nNOS neurons play a role in driving spontaneous hemodynamic fluctuations, but not in setting the basal diameter during different states.

Discussion

We selectively ablated type-I nNOS neurons from the somatosensory cortex, which had marked effects on neural activity and vascular dynamics, but minimal changes in neurovascular coupling. These results are surprising given previous work showing stimulation of these neurons in isolation causes vasodilation and minimal neural activity changes. Our approach of using SP-conjugated saporin allowed a nongenetic means of targeting a critical neuronal cell type, supporting further exploration of the role of type-I nNOS neurons in transgenic mouse models of disease without complicated breeding schemes, as well as in non-model organisms. Our results point to these neurons being an important orchestrator of neural and vascular dynamics, as loss of these neurons causes desynchronization between hemispheres of both neural and vascular signals, as well as altered responses to sensory stimulation. While previous studies using specific activation of type-I nNOS neurons have emphasized the roles of these neurons in driving vasodilation with minimal changes in neural activity, our results point to a larger role of these neurons in organizing and patterning both spontaneous and sensory-evoked neural activity. This is likely due to a loss in NO signaling as well as a loss of the many of the other neuropeptides expressed by type-I nNOS neurons, which all have known effects on other neurons. Loss of type-I nNOS neurons drove minimal changes in the vasodilation elicited by brief stimulation, but led to decreased vascular responses to sustained stimulation,

370 suggesting that the early phase of neurovascular coupling is not mediated by these cells, consistent with the multiple
371 known mechanisms for neurovascular coupling (Attwell et al 2010, Drew 2019, Hosford & Gourine 2019) acting
372 through both neurons and astrocytes with multiple timescales (Le Gac et al 2025, Renden et al 2024, Schulz et al
373 2012, Tran et al 2018).

374 While previous studies have found that activation of type-I nNOS neurons, either optogenetically or via
375 administration of substance P, results in vasodilation (which would imply an important role for these neurons for
376 neurovascular coupling), our work provides insight into the integrated function of type-I nNOS neurons in neural
377 circuits and vascular dynamics. Importantly, methodological approaches differentiate our strategy from previous
378 published work. A limitation of our study is the necessary delay between targeted ablation and in vivo imaging for
379 the animals to recover from surgical procedures. With imaging beginning four weeks after ablation, there could be
380 compensatory rewiring of local and/or network activity following type-I nNOS ablation, where other signaling
381 pathways from the neurons to the vasculature become strengthened to compensate for the loss of vasodilatory
382 signaling from the type-I nNOS neurons. While this likely happens to some degree, this interpretation is less likely to
383 completely account for the effect given these potential compensatory changes do not prevent large changes in
384 neural activity and resting vasomotion. Second, there may be some non-linear interactions between vasodilatory
385 signals and/or the vasodilator mechanisms that are arousal-state-dependent. Intrinsic optical signal readout is
386 primarily weighted toward superficial tissue given the absorption and scattering characteristics of the wavelengths
387 used. While surface vessels are tightly coupled with neural activity, it is still a matter of debate whether surface or
388 intracortical vessels are a more reliable indicator of ongoing activity (Goense et al 2012, Huber et al 2015, Poplawsky
389 & Kim 2014). The diameter of arteries tracks the smooth muscle membrane potential linearly, up until a saturation
390 point above which any hyperpolarization does not induce further dilation (Hill 2012, Knot & Nelson 1998, Wölfle et
391 al 2011). Many vasoactive pathways from neurons to vessels are known to exist, whose individual effects added
392 together sum to larger than observed changes in vasodilation (Hosford & Gourine 2019), suggesting a non-linear
393 interaction. It may be that for dilation occurring during sensory stimulation and sleep, the vasodilatory stimulus to
394 vessels exceeds the saturation point, so that the loss of one vasodilatory pathway does not further affect the vascular
395 response (**Fig. S9**). This would also be consistent with isolated optogenetic or chemical stimulation of type-I nNOS
396 neurons being able to drive substantial dilation, while the loss of these neurons does not have a large impact on the
397 vascular response.

398 Finally, pharmacological ablation and optogenetic/chemogenetic activation are not mirror manipulations and
399 have differences that can produce non-symmetrical changes. Symmetrical changes would only occur if the neural
400 circuitry and the signaling to the vessel were completely linear. Optogenetic activation/deactivation of a single cell
401 type does not produce symmetrical changes in the activity of other neurons (Phillips & Hasenstaub 2016), so there
402 is little reason to think ablation would have the exact opposite effect as activation. Furthermore,
403 optogenetic/pharmacological activation of a single cell type is unlikely to occur endogenously, as neural activity

404 across different cell types is largely correlated (Bugeon et al 2022). For example, during whisker stimulation, not only
405 are type-I nNOS neurons in the somatosensory cortex activated (Ruff et al 2024), but nearly every other cell type is
406 as well (Staiger & Petersen 2021), which mean that type-I nNOS neurons are not the only neurons, and not even the
407 only NO producing neurons, sending signals to the vasculature during sensory stimulation.

408 One surprise is that we observed no changes in the vasodilation during NREM sleep, where type-I nNOS neurons
409 are known to be active and play a role in inducing sleep (Kilduff et al 2011). During NREM sleep, there is marked
410 arterial dilation (Gheres et al 2023, Turner et al 2020), and it would seem natural that type-I nNOS neurons might
411 drive this. However, we saw no difference in NREM dilation between the ablated and control mice. This could be
412 due to compensation, saturation of the vasodilatory response, or it could be due to type-I nNOS neurons releasing
413 other vasoconstrictory peptides (SST, NPY) so their net effects are cancelled out. This last possibility is consistent
414 with the loss of the post-stimulus vasoconstriction seen after type-I nNOS neuron ablation. Again, like with sensory
415 stimulation, there may be a non-linearity in the vascular responses, so that another large factor, such as large
416 neuromodulatory changes during sleep, could dominate over any other vascular signaling factor. The large
417 norepinephrine decreases during NREM (Kjaerby et al 2022, Osorio-Forero et al 2021, Turner et al 2023) could
418 release the vessels from tonic vasoconstriction (as norepinephrine is a vasoconstrictor (Bekar et al 2012)), resulting
419 in the dilation during NREM.

420 Finally, we saw a marked reduction in spontaneous vascular oscillation (vasomotion) at rest, both at the level of
421 single arteries, and at the level of blood volume. These spontaneous oscillations move cerebrospinal fluid (CSF)
422 (Holstein-Ronsbo et al 2023, Kedarasetti et al 2022, van Veluw et al 2020) which is important for clearing waste from
423 the brain, and a reduction in amplitude will decrease the pumping efficacy. Additionally, there is a loss of
424 coordination of neural and vascular dynamics across hemispheres after ablation of type-I nNOS neurons, indicated
425 by the drop in coherence. Although a loss of synchronous dilations/constrictions might affect CSF movement, we
426 might imagine that it would also adversely impact CSF pumping. Aged human brains show reduced interhemispheric
427 synchrony in resting-state signals (Zhao et al 2020), analogous to what we see here. Type-I nNOS neurons also seem
428 uniquely vulnerable to stress (Han et al 2019), and loss of type-I nNOS neurons reduces power in the 1-4Hz band of
429 the LFP, which is positively associated with CSF clearance (Hablitz et al 2019, Jiang-Xie et al 2024). It is possible that
430 adverse life experiences could cause the loss of type-I nNOS neurons, leading to reduction in CSF flow seen in age
431 (Kress et al 2014, Matrongolo et al 2023) that is thought to correlate with neurodegeneration.

432 **Materials and Methods**

433 This study was performed in accordance with the recommendations of the Guide for the Care and Use of
434 Laboratory Animals of the National Institutes of Health. All procedures were performed in accordance with protocols
435 approved by the Institutional Animal Care and Use Committee of Pennsylvania State University (Protocol
436 201042827). Data were acquired from 119 C57BL6/J mice (#000664, The Jackson Laboratory, Bar Harbor, ME)

437 compromised of 57 males and 62 females between 3 and 9 months of age. Previous work from our lab has shown
438 that the vasodilation elicited by whisker stimulation is the same in 2–4-month-old mice as in 18-month-old mice
439 (Bennett et al 2024). As the age range used here is spanned by this time interval, we would not expect any age-
440 related differences. Food and water were provided *ad libitum* and animals were housed on a 12-hr. light/dark cycle
441 with all experiments occurring during the light cycle. Mice were individually housed after surgery. Sample sizes are
442 consistent with previous studies (Echagarruga et al 2020, Turner et al 2023, Turner et al 2020, Zhang et al 2021) and
443 based on a power analysis requiring 8-10 mice per group (Cohen's d = 1.3, $\alpha = 0.05$, $(1 - \beta) = 0.800$. Experimenters
444 were not blind to experimental conditions or data analysis except for histological experiments. Two SP-SAP mice
445 were removed from the imaging datasets (24 SP-SAP remaining) due to not showing ablation of nNOS neurons during
446 post-histological analysis, an attrition rate of approximately 8%.

447 **Surgical Procedures.** Saporin is a ribosome-inactivating protein that was conjugated to the Sar^9, $Met(O_2)^{11}$ analog of
448 Substance P (SP-SAP) or to a control peptide (Blank-SAP) (IT11 & IT21, Advanced Targeting Systems, Carlsbad, CA).
449 Mice were anesthetized using 5% isoflurane (2% maintenance) vaporized in pure oxygen and were then injected
450 intracortically with 4 ng of either SAP conjugate or Blank-SAP in 100 nL of artificial cerebrospinal fluid (aCSF). The
451 incision site was sterilized with betadine and 70% ethanol followed by a retraction of the skin atop the skull. A small
452 (< 0.5 mm) craniotomy was made above the vibrissae representation of somatosensory cortex (2 mm caudal, 3.25
453 mm lateral) and a sterile glass-pulled needle (tip diameter 50-100 µm) was inserted 500 µm beneath the cortical
454 surface at 45°. The SAP conjugate was slowly injected at 100 nL/min using a programmable syringe pump (Harvard
455 Apparatus, Holliston, MA) followed by closure of the incision with VetBond (3M, Saint Paul, MN). A subset of animals
456 were also injected retro-orbitally with 25 µL of AAV PHP.eB-syn-jGCaMP7s-WPRE [$2x10^{13}$ GC/mL] (104487-PHPeB,
457 Addgene, Watertown, MA) diluted in 25 µL of sterile saline. Animals were given at least 2 weeks to recover prior to
458 undergoing additional procedures. For imaging, a custom-machined titanium head bar was adhered atop the
459 occipital bone of the skull using cyanoacrylate glue (Vibra-Tite 32402, ND Industries, Clawson, MI) and dental cement
460 (Ortho-Jet, Lang Dental, Wheeling, IL). Self-tapping 3/32' #000 screws (J.I. Morris, Oxford, MA) were implanted in
461 the frontal bones for structural stability. Electrodes were implanted into cortex and hippocampus using PFA-coated
462 tungsten stereotrodes (#795500, AM systems, Sequim, WA) for recordings of local field potentials (LFP) and into the
463 neck muscles using a pair of PFA-coated 7-strand stainless-steel wires (#793200, AM systems, Sequim, WA) for
464 electromyography (EMG). Polished and reinforced thinned-skull windows (Drew et al., 2010a; Shih et al., 2012b)
465 were implanted over the somatosensory areas (either bilaterally or right hemisphere) using #0 coverslips (#72198,
466 Electron Microscopy Sciences, Hatfield, PA). Detailed surgical procedures are as previously described (Turner et al
467 2020).

468 **Data acquisition.** Data were acquired with a custom LabVIEW program (National Instruments;
469 https://github.com/DrewLab/ LabVIEW-DAQ). Details on widefield optical imaging, two-photon microscopy,
470 electromyography (EMG), electrophysiology, vibrissae stimulation, and behavioral measurements including tracking

471 of vibrissae and pupil diameter were performed as previously described (Turner et al 2023, Turner et al 2020, Zhang
472 et al 2022)). Mice were gradually acclimated to head-fixation of increasing duration (15, 30, 60 minutes) on the days
473 preceding the onset of experiments. The vibrissae (left, right, or a third air puffer not directed at the body as an
474 auditory control) were randomly stimulated with air puffs [0.1 seconds or a train of 5 second pulses, 10 pounds force
475 per square inch (PSI)] occurring every 30–45 seconds for the first 1 hour of imaging. Data were acquired in 15-minute
476 intervals with a brief (~30 seconds) gap in between for saving data to disk. Each animal was run for up to 6 imaging
477 sessions lasting from 1-5 hours depending on experiment. In two-photon experiments, mice were briefly
478 anesthetized and retro-orbitally injected with 100 µL of 5% (weight/volume) fluorescein isothiocyanate–dextran
479 (FITC) (FD150S, Sigma-Aldrich, St. Louis, MO) dissolved in sterile saline. Imaging was done on a Sutter Movable
480 Objective Microscope with a CFI75 LWD 16X W objective (Nikon, Melville, NY) and a MaiTai HP Ti:sapphire laser
481 (Spectra-Physics, Santa Clara, CA) tuned to 800 nm.

482 **Histology.** Following the conclusion of imaging experiments, animals were deeply anesthetized and transcardially
483 perfused with heparin-saline followed by 4% paraformaldehyde. Presence or absence of nNOS-positive neurons in
484 the injected hemisphere was verified using nicotinamide adenine dinucleotide phosphate (NADPH)-diaphorase
485 staining for localizing the sparsely populated type-I nNOS neurons (Scherer-Singler et al 1983).

486 **Immunohistochemistry.** All histological analyses were done blinded to the experimental condition. Mice were
487 deeply anesthetized with 5% isoflurane and perfused transcardially with ice-cold phosphate buffered saline (PBS, pH
488 7.4) and 4% paraformaldehyde (PFA, pH 7.4). Brains were removed, post-fixed in PFA for 24 hours and stored in PBS
489 at 4°C for less than 1 week. A fiduciary mark was placed in the right hemisphere. 40-µm free floating sections were
490 sliced with a Leica vibratome (VS 1200, Leica) and stored in PBS for less than 1 week. Prior to immunostaining, slices
491 were washed three times in PBS for 10 minutes each and underwent antigen retrieval in 10 mM sodium citrate buffer
492 (pH 6.0) at 80°C for 30 minutes. Slices were washed three times in PBS for 10 minutes each, and permeabilized in
493 0.5% Triton X-100 in PBS for 60 minutes. Nonspecific binding was blocked with 5% normal donkey serum (NDS)
494 (ab7475) in 0.1% Triton X-100 in PBS for 60 minutes. Slices were then incubated in a primary antibody cocktail,
495 including goat anti-nNOS (1:500, ab1376), rabbit anti-IBA-1 (1:500, ab178847), rat anti-GFAP (1:500, Thermofisher
496 13-0300), rabbit anti NeuN (1:2000, EnCor), rabbit anti-TACR1 (1:500 Invitrogen PA1-16713) in 2.5% NDS in 0.1%
497 Triton X-100 in PBS for 48-h at 4°C. Slices were rinsed three times with PBS for 10 minutes each, and incubated in a
498 fluorophore-tagged secondary antibody cocktail, including donkey anti-rabbit Alexa Fluor 488 (1:500, ab150073),
499 donkey anti-goat Alexa Fluor 594 (1:500, ab150132), donkey anti rabbit Alexa fluor 647 (1:500, ab150075), donkey
500 anti rat Alexa fluor 488 (1:500 ab150153), for 4 hours at room temperature. Slices were rinsed again three times
501 with PBS, with the last step including DAPI (1:10,000, 10mg/mL, Millpore Sigma, 10236276001), mounted on glass
502 slides, air-dried and cover slipped with Immunomount (Thermo Fisher Scientific, Waltham, MA, United States).
503 Images were obtained with an Olympus BX63 upright microscope (Center Valley, PA, United States) under matched
504 exposure settings. Three to eight images from both hemispheres were taken per region.

505 **Cell counting and immunofluorescence quantification.** Total cell counts and absolute changes in
506 immunofluorescence (**Fig. 1**) were quantified using ImageJ (National Institutes of Health, Bethesda, MD, United
507 States). The region of interest for analysis of cell counts was determined based on the injection site for both SP-SAP
508 and Blank SAP injections, with a 1 mm diameter circle centered around the injection site and averaged across 3-5
509 sections where available. In most animals, the SP-SAP had a lateral spread greater than 500 microns and
510 encompassed the entire depth of cortex (1-1.5 mm in SI). For total cell counts, a region of interest (ROI) was
511 delineated, and cells were automatically quantified under matched criteria for size, circularity and intensity. Image
512 threshold was adjusted until absolute value percentages were between 1-10% of the histogram density. The function
513 *Analyze Particles* was then used to estimate the number of particles with a size of 100-99999 pixels^2 and a
514 circularity between 0.3 and 1.0 (Dao et al 2020, Sicher et al 2023, Smith et al 2020). Immunoreactivity was quantified
515 as mean fluorescence intensity of the ROI (Pleil et al 2015).

516 **Data Analysis.** Data were analyzed with code written by K.L.T, M.S.H, Q.Z, K.W.G, and P.J.D. (MATLAB 2019b–2024a,
517 MathWorks).

518 **Statistical analysis.** Statistical evaluations were made using either generalized linear mixed effects (GLME), unpaired
519 t-test, or general linear model (GLM). GLME models had the arousal state as a fixed effect, mouse identity as a
520 random effect, and hemisphere [left/right (L/R), if applicable] as an interaction with the animal ID, or using a paired
521 t test where appropriate. Unless otherwise stated, statistical results report p values from a GLME test. All reported
522 quantifications are mean ± SD unless otherwise indicated. Unless otherwise noted, all pupil diameter measurements
523 are in z-units. MATLAB functions used were fitglme, ttest, fitglm.

524 **Hemodynamic correction.** Widefield imaging was done with a Dalsa 1M60 Pantera CCD camera (Phase One,
525 Cambridge, MA) with a magnifying lens (VZM 300i, Edmund Optics, Barrington, NJ). Reflectance measurements (**Fig.**
526 **2**) were converted to changes in total hemoglobin (Δ[HbT]), oxy-hemoglobin (Δ[HbO]), and deoxy-hemoglobin
527 (Δ[HbR]) using the Beer–Lambert law (Ma et al., 2016a, b). Correction for attenuation of GCaMP7s fluorescence due
528 to absorption of the surrounding tissue was corrected as previously described (Kramer & Pearlstein 1979, Ma et al
529 2016a, Scott et al 2018, Wright et al 2017). Changes in fluorescence intensity in the GCaMP7s signal due to blood
530 absorption were approximated in a pixel-wise fashion by multiplying each value by the ratio of the green and blue
531 channel's resting baseline pixel value.

532 **Two-photon image processing.** Image stacks were corrected for x-y motion artifacts and aligned with a rigid
533 registration algorithm. A rectangular box was drawn around a straight, evenly-illuminated vessel segment and the
534 pixel intensity was averaged along the long axis to calculate the vessel's diameter from the full-width at half-
535 maximum (https://github.com/DrewLab/Surface-Vessel-FWHM-Diameter; (Drew et al 2011)). The diameter of

536 penetrating arterioles was calculated using the thresholding in Radon space (TiRS) algorithm
537 (https://github.com/DrewLab/Thresholding_in_Radon_Space; (Gao & Drew 2014, Gao et al 2015) .

538 **Electrophysiology.** Gamma-band [30–100Hz] LFP band was digitally bandpass filtered from recorded broadband
539 data using a third-order Butterworth filter, squared, low-pass filtered below 1 Hz, and resampled at 30 Hz. Time-
540 frequency spectrograms (**Fig. 2**) were calculated using the Chronux toolbox version 2.12 v03 (Bokil et al 2010),
541 function mtspecgramc with a 5 s window and 1/5 s step size using [5,9] tapers and a passband of 1–100 Hz to
542 encompass the LFP. EMG (300–3 kHz) from the neck muscles was bandpass filtered, squared, convolved with a
543 Gaussian kernel with a standard deviation of 0.5 seconds, log transformed, then resampled at 30 Hz. MATLAB
544 function(s): butter, zp2sos, filtfilt, gausswin, log10, conv, resample.

545 **Evoked responses and slope.** Evoked responses (**Fig. 3**) including whisker stimulation and locomotion for the various
546 data types ([HbT], [HbO], [HbR], GCaMP7s, arteriole diameter) were compared between the indicated intervals (i.e.,
547 2:4 seconds post-stimulation). The average of the 2 seconds preceding event onsets were subtracted from the event
548 and smoothed with a 3rd order Savitzky-Golay filter. The average slope was calculated by comparing the rise (Δ[HbT])
549 over the run (neural data) before being fit with a linear model forced through the origin. MATLAB function(s):
550 sgolayfilt)

551 **Spectral power and coherence.** Spectral power (**Fig. 4, 5, 6 S5**) was estimated using the Chronux toolbox (Bokil et al
552 2010) function mtspectrumc. Data was detrended within individual events and truncated to the desired length
553 depending on behavior (10 seconds for rest, 15 minutes for Alert and Asleep). Coherence analysis between two
554 signals within the same hemisphere or between signals recorded bilaterally was run for each data type Chronux
555 function coherencyc after detrending using the MATLAB function detrend.

556 **Cross-correlation.** Cross-correlations (**Fig. 5**) between gamma-band power or ΔF/F and changes in total hemoglobin
557 Δ[HbT] were taken during periods of resting-state, alert, and asleep. Data were mean-subtracted and digitally
558 lowpass filtered (< 1 Hz) with a fourth-order Butterworth filter (MATLAB function(s): butter, zp2sos, filtfilt). Cross-
559 correlation analysis was run for each arousal state (MATLAB function(s): xcorr) with a ± 5 second lag time.

560 **Resting-state variance and Δ[HbT] during different arousal states.** Variance during the resting-state for both Δ[HbT]
561 and diameter signals (**Fig. 7**) was taken from resting-state events lasting ≥10 seconds in duration. Average Δ[HbT]
562 from within the 1 mm ROI over the vibrissae representation of SI during each arousal state was taken with respect
563 to awake resting baseline events ≥10 seconds in duration. Continuous NREM sleep events ≥30 seconds, REM sleep
564 events ≥60 seconds, and periods following administration of isoflurane were compared between groups. Each event
565 was digitally lowpass filtered (<1 Hz) with a fourth-order Butterworth filter (MATLAB function(s): butter, zp2sos,
566 filtfilt) and then averaged within each individual time series prior to comparing across animals/groups.

Open field behavior. Exploratory behavior (**Fig. S2)** was measured in a custom-made 30 cm x 60 cm arena during the light phase. Mice were not habituated to the arena. Mice were placed in the arena for 10 minutes to explore, and their behavior was recorded using an overhead camera (Blackfly BFLY-U3-23S6M, Teledyne FLIR, Wilsonville, OR) with 6 mm fixed focal length lens (Edmund Optics, Barrington, NJ, Stock #33939) at a frame rate of either 15 or 30 frames per second. The arena was illuminated with 780nm light. The surroundings of the arena were dark during the entire recording session. The arena was cleaned with 70% ethanol in between animals. Only the first 5 minutes of the behavior were analyzed and reported here. The total distance traveled over the first 5 minutes, and the time spent in the 25 x 55 cm center rectangle was quantified. Generalized linear mixed effect (GLME) was used in MATLAB to perform statistical analysis. No statistical outliers were removed from the data. Mouse behavior was tracked using DeepLabCut (Mathis et al 2018) and analyzed with custom MATLAB algorithms (Brockway et al 2023, Zhang et al 2022). Eight points on the body (left ear, right ear, head, mid, back near the hip joint, base of the tail, midpoint of the tail, and end of the tail) were tracked. Four markers placed in the arena's four corners with an additional four points calculated from the four corners to track the center rectangle. A DeepLabCut model was trained and evaluated on a subset of mice before applying the model to all the mice. DeepLabCut tracking was considered acceptable if the tracking confidence was above 97%; however, in most cases, it was higher than 99%. Tracking positions were exported to a CSV file containing the tracked location's XY coordinates (frame pixels). Tracked videos from random mice were visualized to confirm the accuracy of the tracking. The experimenter was blinded to drug injection group identification until tracking and analysis were completed. The distance was calculated from the first 5 minutes as Euclidean distance between the point tracked in the middle of the mouse body from subsequent frames. Center time was quantified as the number of frames a mouse spends within the polygon bounded by 4 points tracked on the center of the arena.

Sleep scoring. Sleep scoring (**Fig. S3**) was performed as in Turner et al. (2020). Briefly, arousal state was scored using a combination of cortical and hippocampal LFP, EMG, pupil diameter, and whisker and body moment. Periods of manually chosen awake rest 5s in duration with no vibrissae or body motion were used as a baseline to normalize neural and hemodynamic signals. NREM sleep shows elevated cortical delta-band power and lower EMG power. REM sleep is marked by elevated hippocampal theta-band power and elevated cortical gamma-band power with very low baseline EMG power (muscle atonia; Cantero et al., 2004; Montgomery et al., 2008; Le Van Quyen et al., 2010; Sullivan et al., 2014). Every 5 second interval was classified as either Awake, NREM sleep, or REM sleep using a bootstrap aggregating random forest model with the predictors of cortical delta band power, cortical beta band power, cortical gamma LFP, hippocampal theta LFP, EMG power, heart rate, and whisking duration. Sleep model accuracy was validated using the out-of-bag error during model training. MATLAB functions used were TreeBagger, oobError, predict.

Pupil diameter and interblink interval. Pupil diameter (**Fig. S2**) was lowpass filtered at 1 Hz with a fourth-order Butterworth filter. Changes in whisking-evoked and stimulus-evoked (contralateral, auditory) diameters normalized relative to the mean of the 2 second preceding the event onset. MATLAB functions used were butter, zp2sos, filtfilt. Interblink interval and blink-associated physiology. Because of breaks in recording to save the data to disk, interblink interval was calculated between blinks occurring within 15 min records and not blinks on the edges of trials. Blinks that occurred within 1 second of each other were linked together as blinking bouts, and all blink-triggered analyses were with respect to the first blink in a series. Blink-triggered averages were separated into two groups depending on the arousal state classification of the 5 second bin before the blink, being either Awake (arousal state classification of Awake) or Asleep (arousal state classification being either NREM or REM).

Hemodynamic response function. The hemodynamic response function (HRF, **Fig. S5**) was calculated as previously described (Winder et al 2017, Zhang et al 2023) using both deconvolution and fitting the response to a gamma distribution. Only neural activity (gamma-band power, 30-100 Hz) within 1.5 second of the stimulus was used for calculating the HRF. Each HRF was calculated using half of the data and tested on the other half. To test the predictive capability of each HRF, the impulse function was fit with a gamma-distribution function and convolved with the neural power to predict the measured hemodynamic signal. The coefficient of determination (R^2) between the predicted and actual hemodynamic signal was evaluated to quantify the efficacy of HRF's prediction (MATLAB function(s): sgolayfilt, detrend, fminsearch, fitlm).

Pearson's correlation coefficient calculations. The Pearson's correlation coefficient between bilateral signals (**Fig. S6**) was obtained by mean-subtracting and digitally lowpass filtering (<1 Hz) with a fourth-order Butterworth filter and then taking the Pearson's correlation coefficient (MATLAB function(s): butter, zp2sos, filtfilt, corrcoef).

Arousal state transitions. Transitions between arousal states (Awake to NREM, NREM to Awaken, NREM to REM, REM to Awake) were compared across groups (**Fig. S8**) by averaging events that met the criteria of 30 seconds of one state's consecutive classifications followed by 30 seconds of another state. The difference in the Δ[HbT] between the pre- and post- state transition were compared by taking the 30:10 seconds prior to the transition zero point to the 10:30 seconds following. [HbT] was digitally lowpass (<1 Hz) filtered using a fourth-order Butterworth filter (MATLAB function(s): butter, zp2sos, filtfilt).

Data availability. Data and code for generating the figures are available at https://datadryad.org/dataset/doi:10.5061/dryad.tb2rbp0bq and analysis code is available at https://github.com/KL-Turner/Turner-eLife2025. Raw data is available upon reasonable request.

629 **Supplemental Figure 1**

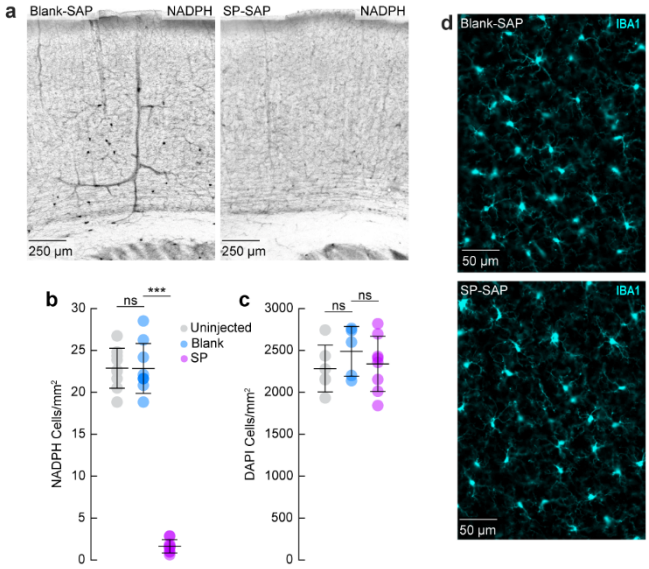

Figure S1. Histological quantification of cortical SP-Sap injections (a) Examples of NADPH diaphorase staining from Blank-SAP and SP-SAP injected mice. **(b)** SP-SAP injected mice (N = 9, 5M/4F) had significantly lower numbers of type-I nNOS cells than either Blank-SAP (N = 9, 4M/5F) or Uninjected mice (N = 9, 4M/5F) (SP-SAP: 1.6 ± 0.8 neurons/mm^2; Blank-SAP: 22.9 ± 2.4 neurons/mm^2; Uninjected: 22.9 ± 3 neurons/mm^2; Blank-SAP vs. Uninjected: p = 0.98; Blank-SAP vs. SP-SAP: p = 2.23×10^{-13}). **(c)** Counts of DAPI-labeled cell nuclei per square mm from imaged mice. Uninjected (N = 6, 6M) mice had 2284 ± 279 DAPI-labeled cell bodies/mm^2, which was not significantly different than those injected with Blank-SAP (N = 5, 5F, 2488 ± 298, *p* = 0.23, GLME), which in turn was not significantly different than those injected with SP-SAP (N = 8, 4M/4F, 2340 ± 329, *p* = 0.39, GLME. **(d)** Representative image of IBA1 for Blank-SAP (top) and SP-SAP (bottom) taken from **Fig 1c**. Error bars (**b, c**) denote SD. *α < 0.05, **α < 0.01, ***α < 0.001, GLME.

Supplemental Figure 2

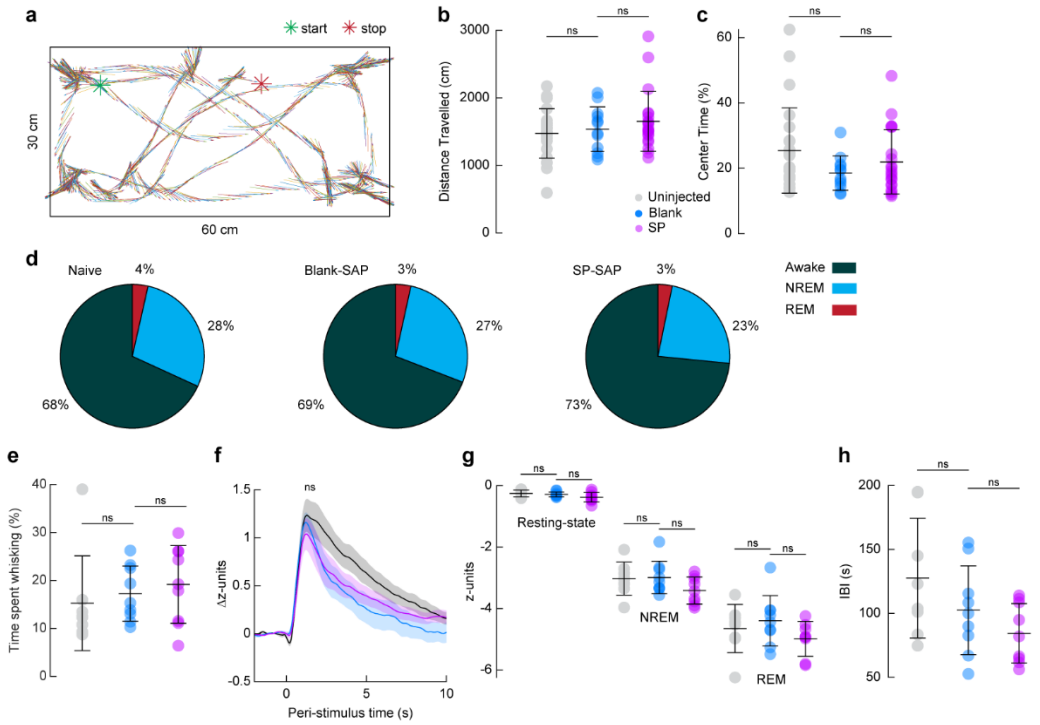

Figure S2. Behavior was unaffected by local ablation of type-I nNOS neurons (a) Example of exploratory behavior during 5 minutes of exploration in a novel environment. **(b)** Total distance traveled during open field exploration. Uninjected mice traveled an average of 1473.4 ± 364.7 cm compared with 1536.6 ± 329.6 cm in Blank-SAP (p = 0.61) and 1652.3 ± 442.7 cm in SP-SAP (p = 0.43). **(c)** Time spent in the center of the open field. Uninjected mice spent on average 25.5 ± 13.1% of total exploration time in the center compared with 18.5 ± 5.3% in Blank-SAP (p = 0.08, GLME) and 21.9 ±9.8% in SP-SAP (p = 0.26). **(b, c)** n = 12-23 mice per group. **(d)** Percentage of time classified in each arousal state by sleep scoring. Uninjected mice spent 68.1 ± 13.2% of the time awake compared to 69.1 ± 15.1% in Blank-SAP (p = 0.89, ttest) and 73.4 ± 11.6% in SP-SAP (p = 0.51, ttest). Uninjected mice spent 28.3 ± 11.1% of the time in NREM sleep compared to 27.4 ± 12.0% in Blank-SAP (p = 0.87, ttest) and 23.4 ± 9.7% in SP-SAP (p = 0.44, ttest). Uninjected mice spent 3.5 ± 2.9% of the time in REM sleep compared to 3.4 ± 3.5% in Blank-SAP (p = 0.96, ttest) and 3.2 ± 2.3% in SP-SAP (p = 0.88, ttest). **(e)** Time spent whisking as a percentage of total imaging time. Uninjected mice spent 15.3 ± 9.9% compared with 17.3 ± 5.8% in Blank-SAP (p = 0.61, ttest) and 19.2 ± 8.1% in SP-SAP (p = 0.75, ttest). **(f)** Change in Pupil diameter in response to vibrissae stimulation. Pupil diameter of uninjected mice increased 1.3 ± 0.5 z-units following vibrissae stimulation compared with 1.2 ± 0.3 z-units in Blank-SAP (p = 0.76, ttest) and 1.1 ± 0.5 z-units in SP-SAP (p = 0.50, ttest). **(g)** Average pupil diameter across arousal states. Average pupil diameter of Uninjected mice during the resting-state was -0.25 ± 0.1 z-units compared with -0.29 ± 0.1 z-units in Blank-SAP (p = 0.45, ttest) and -0.34 ± 0.2 in SP-SAP (p = 0.14, ttest). Average pupil diameter of Uninjected mice during periods of NREM sleep was -3 ± 0.5 z-units compared with -3 ± 0.5 z-units in Blank-SAP (p = 0.89, ttest) and -3.4 ± 0.4 in SP-SAP (p = 0.08, ttest). Average pupil diameter of Uninjected mice during periods of REM sleep was -4.6 ± 0.8 z-units compared with -4.4 ± 0.8 z-units in Blank-SAP (p = 0.53, ttest) and -5 ± 0.6 in SP-SAP (p = 0.11, ttest) **(h)** Interblink-interval. Uninjected mice had a mean interblink-interval of 127.6 ± 46.8 s compared with 102.5 ± 34.7 s in Blank-SAP (p = 0.22, ttest) and 84.5 ± 23.3 s in SP-SAP (p = 0.21, ttest). **(d-h)** n = 9 mice per group. Shading **(f)** indicates SEM and error bars **(b, c, e, g, h)** denote SD. *α < 0.05, **α < 0.01, ***α < 0.001.

631 **Supplemental Figure 3**

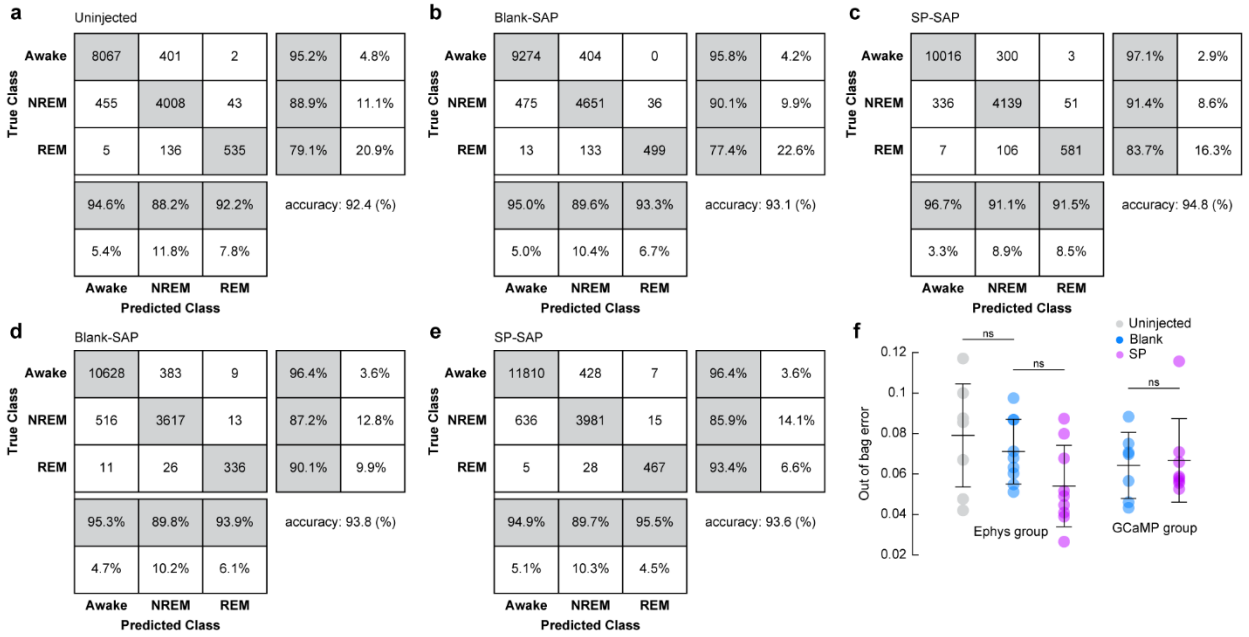

Figure S3. Sleep classification accuracy was unchanged following type-I nNOS ablation (a) Confusion matrix for arousal state classification of Uninjected mice with bilaterally implanted stereotrodes. **(b)** Confusion matrix for arousal state classification of Blank-SAP mice with bilaterally implanted stereotrodes. **(c)** Confusion matrix for arousal state classification of SP-SAP mice with bilaterally implanted stereotrodes. **(a-c)** n = 9 mice per group. **(d)** Confusion matrix for arousal state classification of Blank-SAP mice expressing pan-neuronal GCaMP. **(e)** Confusion matrix for arousal state classification of SP-SAP mice expressing pan-neuronal GCaMP. **(d, e)** n = 6-7 mice per group. **(f)** Out-of-bag error during training of each animal's bootstrapped random forest classification algorithm. For mice with bilateral LFP recordings, Uninjected mice had an average loss of 0.08 ± 0.03 in comparison to 0.07 ± 0.02 in Blank-SAP (p = 0.45, ttest) compared to 0.05 ± 0.02 in SP-SAP (p = 0.064, ttest). Blank-SAP mice with pan-neuronal GCaMP had an average classification loss of 0.06 ± 0.02 compared with 0.07 ± 0.02 in SP-SAP (p = 0.80, ttest). Error bars denote SD. *α < 0.05, **α < 0.01, ***α < 0.001.

632 **Supplemental Figure 4**

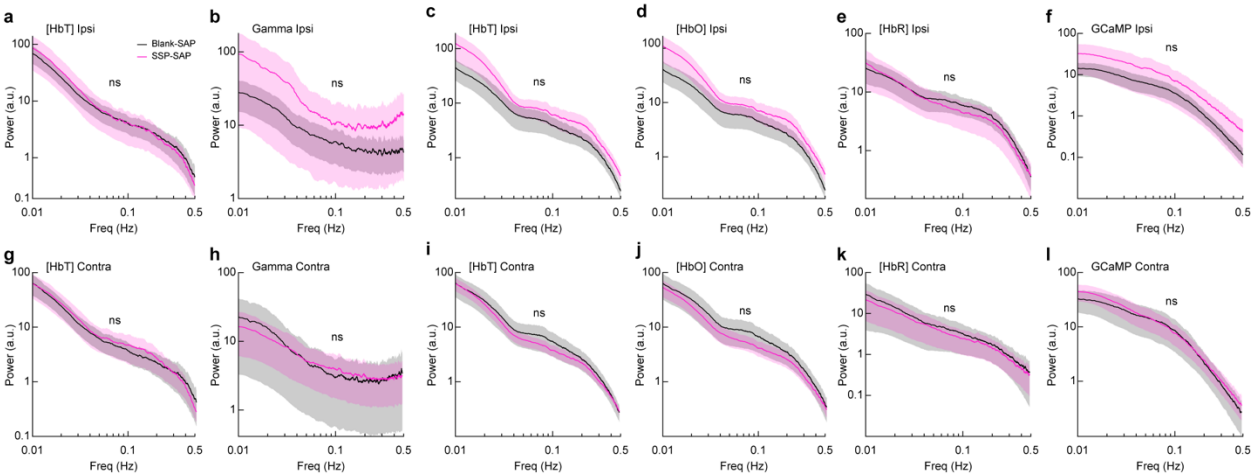

Figure S4. Ablation of Type-I nNOS neurons does not alter hemodynamic or neural power spectra Power spectral density for vascular and hemodynamic signals for the Blank-SAP group (N = 9, 4M/5F for **a, b, g, h**; N = 7, 3M/4F for **c-f; i-l**) and SP-SAP group (N = 9, 5M/4F for **a, b, g, h;** N = 8, 4M/4F for **c-f; i-l**) was not significantly different across all measurements of hemodynamic and neural signals in the injected (ipsilateral) hemisphere **(a-f)** or in the un-injected (contralateral) hemisphere **(g-l)**. **(a)** Δ[HbT] for electrophysiology animals (p = 0.65, GLME). **(b)** Gamma-band power (second spectra) for animals with electrophysiology (p = 0.47, GLME). **(c)** Δ[HbT] for animals with GCaMP (p = 0.27, GLME). **(d)** Δ[HbT] for animals with GCaMP (p = 0.27, GLME). **(e)** Δ[HbT] for animals with GCaMP (p = 0.97, GLME). **(f)** GCaMP fluorescence (p = 0.48, GLME). **(g)** Δ[HbT] for electrophysiology animals (p = 0.80, GLME). **(h)** Gamma-band power (second spectra) for animals with electrophysiology (p = 0.95, GLME). **(i)** Δ[HbT] for animals with GCaMP (p = 0.83, GLME). **(j)** Δ[HbT] for animals with GCaMP (p = 0.69, GLME). **(k)** Δ[HbT] for animals with GCaMP (p = 0.87, GLME). **(l)** GCaMP fluorescence (p = 0.82, GLME). Shading represents population averages ± SEM. *$\alpha < 0.05$, **$\alpha < 0.01$, ***$\alpha < 0.001$.

633 **Supplemental Figure 5**

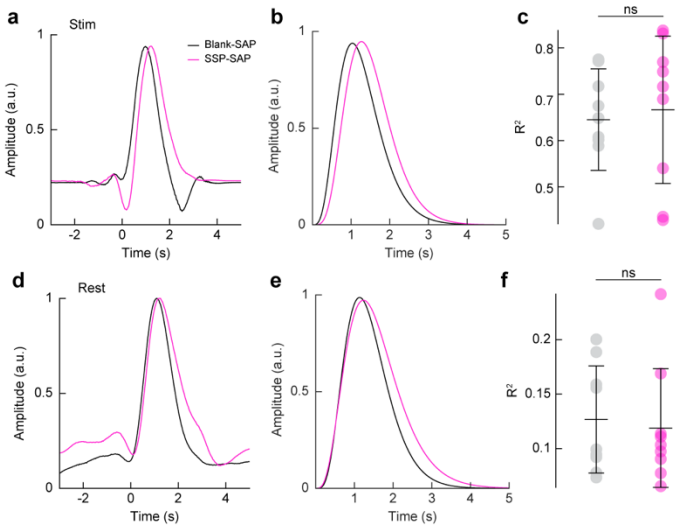

Figure S5. Ablation of Type-I nNOS neurons does not alter the predictive power of the hemodynamic response function (a) Stimulus-evoked hemodynamic response function obtained with deconvolution. **(b)** Stimulus-evoked hemodynamic response function fitted with a gamma distribution function. **(c)** There was no significant difference between the Δ[HbT] predictive R^2 values calculated from impulse-derived HRFs between Blank-SAP (N = 9, 4M/5F) 0.64 ± 0.11 or SP-SAP (N = 9, 5M/4F) 0.67 ± 0.16 following vibrissae stimulation (p = 0.746, ttest). **(d)** Resting-state hemodynamic response function based on deconvolution. **(e)** Resting-state hemodynamic response function fitted with a gamma distribution function. **(f)** There was no significant difference between the Δ[HbT] predictive R^2 values calculated from impulse-derived HRFs between Blank-SAP (N = 9, 4M/5F) 0.13 ± 0.0.05 or SP-SAP (N = 9, 5M/4F) 0.12 ± 0.05 during the resting-state (p = 0.749, ttest). Error bars denote SD. *α < 0.05, **α < 0.01, ***α < 0.001.

634 **Supplemental Figure 6**

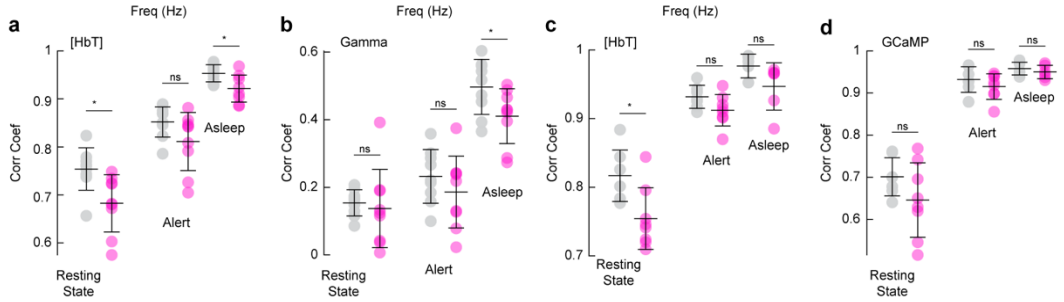

Figure S6. Pearson's correlation coefficients between bilateral hemodynamic and neural signals (a) Correlation coefficient between bilateral hemodynamic signals during the resting-state was 0.75 ± 0.04 in Blank-SAP and 0.68 ± 0.06 in SP-SAP (ttest p = 0.011), during the alert state was 0.85 ± 0.03 with Blank-SAP and 0.81 ± 0.06 in SP-SAP (ttest p = 0.09), and during the asleep state was 0.95 ± 0.02 in Blank-SAP and 0.92 ± 0.03 in SP-SAP (ttest p = 0.01). **(b)** Correlation coefficient between bilateral gamma-band power signals during the resting-state was 0.15 ± 0.04 in Blank-SAP and 0.14 ± 0.12 in SP-SAP (ttest p = 0.69), during the alert state was 0.23 ± 0.08 in Blank-SAP and 0.19 ± 0.11 in SP-SAP (ttest p = 0.31), and during the asleep state was 0.50 ± 0.08 in Blank-SAP and 0.41 ± 0.08 in SP-SAP (ttest p = 0.04). **(c)** Correlation coefficient between bilateral hemodynamic signals (GCaMP7s group) during the resting-state was 0.82 ± 0.04 in Blank-SAP and 0.75 ± 0.04 in SP-SAP (ttest p = 0.01), during the alert state was 0.93 ± 0.02 in Blank-SAP and 0.91 ± 0.02 in SP-SAP (ttest p = 0.08), and during the asleep state was 0.98 ± 0.02 with SP-SAP and 0.95 ± 0.03 in SP-SAP (ttest p = 0.07). **(d)** Correlation coefficient between bilateral GCaMP7s signals during the resting-state was 0.70 ± 0.05 in Blank-SAP and 0.65 ± 0.09 in SP-SAP (ttest p = 0.16), during the alert state was 0.93 ± 0.03 with Blank-SAP and 0.92 ± 0.03 in SP-SAP (ttest p = 0.31), and during the asleep state was 0.96 ± 0.02 with Blank-SAP and 0.95 ± 0.02 in SP-SAP (ttest p = 0.37). Error bars denote SD. $\alpha < 0.05$, $^{**}\alpha < 0.01$, $^{***}\alpha < 0.001$.

635 **Supplemental Figure 7**

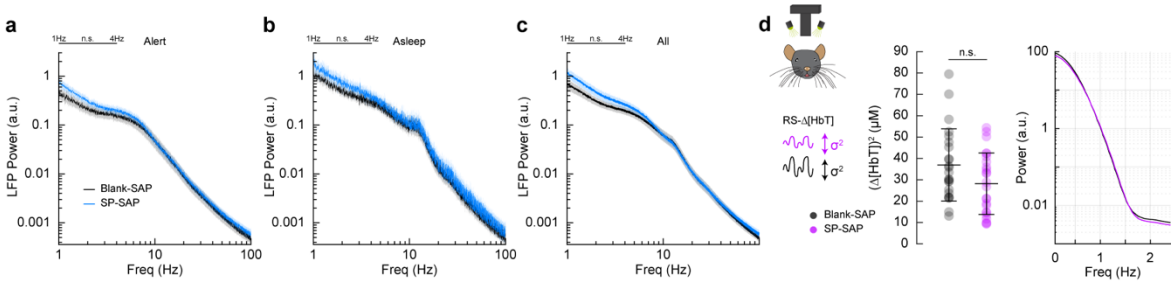

Figure S7. Ablation of Type-I nNOS neurons does not alter LFP or vasomotion in the contralateral hemisphere (a) The power in the delta-band of the LFP in Blank-SAP mice (N = 9, 4M/5F) in the alert state (Fig. 4a) was $1.6\times10^{-10} \pm 2.4\times10^{-11}$ a.u. compared to $2.1\times10^{-10} \pm 2.5\times10^{-11}$ a.u. in the SP-SAP mice (N = 9, 5M/4F, GLME $p = 0.14$). **(b)** The power in the delta-band of the LFP in Blank-SAP mice (N = 7, 3M/4F) in the asleep state was (NREM + REM) was $3.2\times10^{-10} \pm 3.3\times10^{-11}$ a.u. compared to $4.4\times10^{-10} \pm 9.7\times10^{-11}$ a.u. in the SP-SAP mice (N = 7, 4M/3F, GLME $p = 0.18$). **(c)** The power in the delta-band of the LFP in Blank-SAP mice (N = 9, 4M/5F) averaged across all arousal states was $2.1\times10^{-10} \pm 3.1\times10^{-10}$ a.u. compared to $3.1\times10^{-10} \pm 5.0\times10^{-11}$ a. u. in the SP-SAP mice (N = 9, 5M/4F, GLME $p = 0.11$). **(d)** The variance in Δ[HbT] during rest, a measure of vasomotion amplitude, was not significantly reduced in the un-injected (contralateral) hemisphere following type-I nNOS ablation; dropping from 36.9 ± 3.4 μM^2 in the Blank-SAP group (N = 16, 7M/9F) to 28.2 ± 2.9 μM^2 in the SP-SAP group (N = 17, 9M/8F) (GLME $p = 0.06$). Shading represents population averages ± SEM. *$\alpha < 0.05$, **$\alpha < 0.01$, ***$\alpha < 0.001$.

Supplemental Figure 8

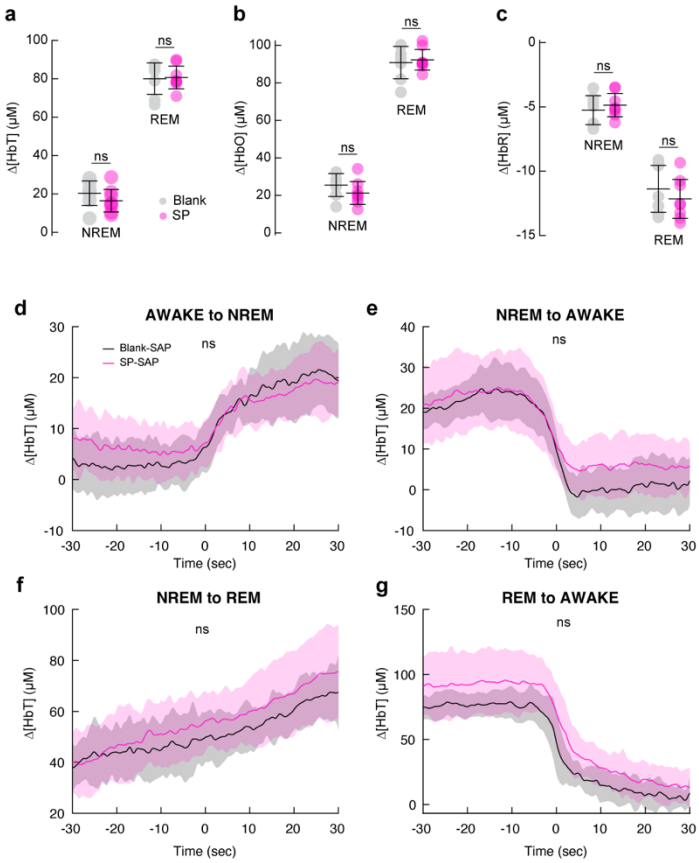

Figure S8. Removal of type-I nNOS neurons did not alter arousal state-related hemodynamic changes (a-c) Average Δ[HbT/O/R] during periods of NREM sleep and REM sleep in mice with pan-neuronal GCaMP (n = 6-7 mice per group). **(a)** NREM Δ[HbT] in Blank-SAP mice was 20.4 ± 6.4 μM compared to 16.5 ± 5.9 μM in SP-SAP (p = 0.27, ttest). REM Δ[HbT] in Blank-SAP mice was 80.0 ± 8.2 μM compared to 80.7 ± 5.9 μM in SP-SAP (p = 0.87, ttest). **(b)** NREM Δ[HbO] in Blank-SAP mice was 25.5 ± 6.1 μM compared to 21.2 ± 6.1 μM in SP-SAP (p = 0.23, ttest). REM Δ[HbO] in Blank-SAP mice was 90.8 ± 8.6 μM compared to 92.3 ± 5.5 μM in SP-SAP (p = 0.72, ttest). **(c)** NREM Δ[HbR] in Blank-SAP mice was -5.3 ± 1.1 μM compared to -4.9 ± 0.9 μM in SP-SAP (p = 0.50, ttest). REM Δ[HbR] in Blank-SAP mice was -11.4 ± 1.8 μM compared to -12.2 ± 1.5 μM in SP-SAP (p = 0.42, ttest). **(d)** Transition from Awake to NREM had a Δ[HbT] of -16.6 ± 6.4 μM in Blank-SAP mice and -11.1 ± 7.0 μM in SP-SAP mice ($p < 0.08$, GLME). **(e)** Transition from NREM to Awake had a Δ[HbT] of 21.5 ± 7.7 μM in Blank-SAP mice and 17.6 ± 9.5 μM in SP-SAP mice ($p < 0.33$, GLME). **(f)** Transition from NREM to REM had a Δ[HbT] of -17.6 ± 3.9 μM in Blank-SAP mice and -22.6 ± 7.9 μM in SP-SAP mice ($p < 0.09$, GLME). **(g)** Transition from REM to Awake had a Δ[HbT] of 67.8 ± 7.3 μM in Blank-SAP mice and 74.0 ± 13.1 μM in SP-SAP mice ($p < 0.21$, GLME). Error bars denote SD. Shading represents population averages ± SEM.*$\alpha < 0.05$, **$\alpha < 0.01$, ***$\alpha < 0.001$.

637 **Supplemental Figure 9**

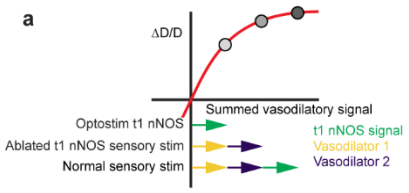

Figure S9. Schematic showing how non-linearity in the dilation response can explain coexistence strong dilation by activation of a pathway, and little change after weakening a pathway. If the diameter is a sublinear function of the sum of vasodilatory inputs, activation of all pathways will cause a dilation that is smaller than the sum of activation of each pathway individually. Loss of one pathway will not cause large changes, even though activation of that pathway in isolation can cause large dilations.

638 **References**

639 Abbott SB, Kanbar R, Bochorishvili G, Coates MB, Stornetta RL, Guyenet PG. 2012. C1 neurons excite locus coeruleus
640 and A5 noradrenergic neurons along with sympathetic outflow in rats. *J Physiol* 590: 2897-915

641 Ahn SJ, Anfray A, Anrather J, Iadecola C. 2023. Calcium transients in nNOS neurons underlie distinct phases of the
642 neurovascular response to barrel cortex activation in awake mice. *J Cereb Blood Flow Metab*:
643 271678X231173175

644 Andrei AR, Debes S, Chelaru M, Liu X, Rodarte E, et al. 2021. Heterogeneous side effects of cortical inactivation in
645 behaving animals. *Elife* 10

646 Attwell D, Buchan AM, Charpak S, Lauritzen M, Macvicar BA, Newman EA. 2010. Glial and neuronal control of brain
647 blood flow. *Nature* 468: 232-43

648 Bekar LK, Wei HS, Nedergaard M. 2012. The locus coeruleus-norepinephrine network optimizes coupling of cerebral
649 blood volume with oxygen demand. *Journal of Cerebral Blood Flow & Metabolism* 32: 2135-45

650 Bennett HC, Zhang Q, Wu YT, Manjila SB, Chon U, et al. 2024. Aging drives cerebrovascular network remodeling and
651 functional changes in the mouse brain. *Nat Commun* 15: 6398

652 Bergamaschi G, Perfetti V, Tonon L, Novella A, Lucotti C, et al. 1996. Saporin, a ribosome-inactivating protein used
653 to prepare immunotoxins, induces cell death via apoptosis. *Br J Haematol* 93: 789-94

654 Bokil H, Andrews P, Kulkarni JE, Mehta S, Mitra PP. 2010. Chronux: a platform for analyzing neural signals. *J Neurosci*
655 *Methods* 192: 146-51

656 Bredt DS, Glatt CE, Hwang PM, Fotuhi M, Dawson TM, Snyder SH. 1991. Nitric oxide synthase protein and mRNA are
657 discretely localized in neuronal populations of the mammalian CNS together with NADPH diaphorase.
658 *Neuron* 7: 615-24

659 Brockway DF, Griffith KR, Aloimonos CM, Clarity TT, Moyer JB, et al. 2023. Somatostatin peptide signaling dampens
660 cortical circuits and promotes exploratory behavior. *Cell Rep* 42: 112976

661 Bugeon S, Duffield J, Dipoppa M, Ritoux A, Prankerd I, et al. 2022. A transcriptomic axis predicts state modulation of
662 cortical interneurons. *Nature* 607: 330-38

663 Cardin JA, Carlen M, Meletis K, Knoblich U, Zhang F, et al. 2009. Driving fast-spiking cells induces gamma rhythm and
664 controls sensory responses. *Nature* 459: 663-7

665 Chan KY, Jang MJ, Yoo BB, Greenbaum A, Ravi N, et al. 2017. Engineered AAVs for efficient noninvasive gene delivery
666 to the central and peripheral nervous systems. *Nat Neurosci* 20: 1172-79

667 Chong PS, Poon CH, Fung ML, Guan L, Steinbusch HWM, et al. 2019. Distribution of neuronal nitric oxide synthase
668 immunoreactivity in adult male Sprague-Dawley rat brain. *Acta Histochem* 121: 151437

669 Claron J, Provansal M, Salardaine Q, Tissier P, Dizeux A, et al. 2023. Co-variations of cerebral blood volume and single
670 neurons discharge during resting state and visual cognitive tasks in non-human primates. *Cell Rep* 42:
671 112369

672 Dana H, Sun Y, Mohar B, Hulse BK, Kerlin AM, et al. 2019. High-performance calcium sensors for imaging activity in
673 neuronal populations and microcompartments. *Nat Methods* 16: 649-57

674 Dao NC, Suresh Nair M, Magee SN, Moyer JB, Sendao V, et al. 2020. Forced Abstinence From Alcohol Induces Sex-
675 Specific Depression-Like Behavioral and Neural Adaptations in Somatostatin Neurons in Cortical and
676 Amygdalar Regions. *Front Behav Neurosci* 14: 86

677 Dittrich L, Heiss JE, Warrier DR, Perez XA, Quik M, Kilduff TS. 2012. Cortical nNOS neurons co-express the NK1
678 receptor and are depolarized by Substance P in multiple mammalian species. *Front Neural Circuits* 6: 31

679 Dittrich L, Morairty SR, Warrier DR, Kilduff TS. 2015. Homeostatic sleep pressure is the primary factor for activation
680 of cortical nNOS/NK1 neurons. *Neuropsychopharmacology* 40: 632-9

681 Drew PJ. 2019. Vascular and neural basis of the BOLD signal. *Curr Opin Neurobiol* 58: 61-69

682 Drew PJ, Shih AY, Driscoll JD, Knutsen PM, Blinder P, et al. 2010. Chronic optical access through a polished and
683 reinforced thinned skull. *Nat Methods* 7: 981-4

684 Drew PJ, Shih AY, Kleinfeld D. 2011. Fluctuating and sensory-induced vasodynamics in rodent cortex extend arteriole
685 capacity. *Proc Natl Acad Sci U S A* 108: 8473-8

686 Drew PJ, Winder AT, Zhang Q. 2019. Twitches, Blinks, and Fidgets: Important Generators of Ongoing Neural Activity.
687 *Neuroscientist* 25: 298-313

688 Echagarruga CT, Gheres KW, Norwood JN, Drew PJ. 2020. nNOS-expressing interneurons control basal and
689 behaviorally evoked arterial dilation in somatosensory cortex of mice. *Elife* 9

690 Endo T, Yanagawa Y, Komatsu Y. 2016. Substance P Activates Ca2+-Permeable Nonselective Cation Channels through
691 a Phosphatidylcholine-Specific Phospholipase C Signaling Pathway in nNOS-Expressing GABAergic Neurons
692 in Visual Cortex. *Cereb Cortex* 26: 669-82

693 Gao YR, Drew PJ. 2014. Determination of vessel cross-sectional area by thresholding in Radon space. *J Cereb Blood*
694 *Flow Metab* 34: 1180-7

695 Gao YR, Greene SE, Drew PJ. 2015. Mechanical restriction of intracortical vessel dilation by brain tissue sculpts the
696 hemodynamic response. *Neuroimage* 115: 162-76

697 Gerashchenko D, Schmidt MA, Zielinski MR, Moore ME, Wisor JP. 2018. Sleep State Dependence of Optogenetically
698 evoked Responses in Neuronal Nitric Oxide Synthase-positive Cells of the Cerebral Cortex. *Neuroscience*
699 379: 189-201

700 Gerashchenko D, Wisor JP, Burns D, Reh RK, Shiromani PJ, et al. 2008. Identification of a population of sleep-active
701 cerebral cortex neurons. *Proc Natl Acad Sci U S A* 105: 10227-32

702 Gheres KW, Unsal HS, Han X, Zhang Q, Turner KL, et al. 2023. Arousal state transitions occlude sensory-evoked
703 neurovascular coupling in neonatal mice. *Commun Biol* 6: 738

704 Goense J, Merkle H, Logothetis NK. 2012. High-resolution fMRI reveals laminar differences in neurovascular coupling
705 between positive and negative BOLD responses. *Neuron* 76: 629-39

706 Hablitz LM, Vinitsky HS, Sun Q, Staeger FF, Sigurdsson B, et al. 2019. Increased glymphatic influx is correlated with
707 high EEG delta power and low heart rate in mice under anesthesia. *Sci Adv* 5: eaav5447

708 Han K, Min J, Lee M, Kang BM, Park T, et al. 2019. Neurovascular Coupling under Chronic Stress Is Modified by Altered
709 GABAergic Interneuron Activity. *J Neurosci* 39: 10081-95

710 Haselden WD, Kedarasetti RT, Drew PJ. 2020. Spatial and temporal patterns of nitric oxide diffusion and degradation
711 drive emergent cerebrovascular dynamics. *PLoS Comput Biol* 16: e1008069

712 He M, Tucciarone J, Lee S, Nigro MJ, Kim Y, et al. 2016. Strategies and Tools for Combinatorial Targeting of GABAergic
713 Neurons in Mouse Cerebral Cortex. *Neuron* 91: 1228-43

714 Hendry SH, Schwark HD, Jones EG, Yan J. 1987. Numbers and proportions of GABA-immunoreactive neurons in
715 different areas of monkey cerebral cortex. *J Neurosci* 7: 1503-19

716 Higo S, Udaka N, Tamamaki N. 2007. Long-range GABAergic projection neurons in the cat neocortex. *J Comp Neurol*
717 503: 421-31

718 Hill CE. 2012. Long Distance Conduction of Vasodilation: A Passive or Regenerative Process? *Microcirculation* 19:
719 379-90

720 Holstein-Ronsbo S, Gan Y, Giannetto MJ, Rasmussen MK, Sigurdsson B, et al. 2023. Glymphatic influx and clearance
721 are accelerated by neurovascular coupling. *Nat Neurosci*

722 Hope BT, Michael GJ, Knigge KM, Vincent SR. 1991. Neuronal NADPH diaphorase is a nitric oxide synthase. *Proc Natl*
723 *Acad Sci U S A* 88: 2811-4

724 Hope BT, Vincent SR. 1989. Histochemical characterization of neuronal NADPH-diaphorase. *J Histochem Cytochem*
725 37: 653-61

726 Hosford PS, Gourine AV. 2019. What is the key mediator of the neurovascular coupling response? *Neurosci Biobehav*
727 *Rev* 96: 174-81

728 Huang H, Kuzirian MS, Cai X, Snyder LM, Cohen J, et al. 2016. Generation of a NK1R-CreER knockin mouse strain to
729 study cells involved in Neurokinin 1 Receptor signaling. *Genesis* 54: 593-601

730 Huber L, Goense J, Kennerley AJ, Trampel R, Guidi M, et al. 2015. Cortical lamina-dependent blood volume changes
731 in human brain at 7 T. *Neuroimage* 107: 23-33

732 Huo BX, Gao YR, Drew PJ. 2015. Quantitative separation of arterial and venous cerebral blood volume increases
733 during voluntary locomotion. *Neuroimage* 105: 369-79

734 Huo BX, Smith JB, Drew PJ. 2014. Neurovascular coupling and decoupling in the cortex during voluntary locomotion.
735 *J Neurosci* 34: 10975-81

736 Iadecola C, Smith EE, Anrather J, Gu C, Mishra A, et al. 2023. The Neurovasculome: Key Roles in Brain Health and
737 Cognitive Impairment: A Scientific Statement From the American Heart Association/American Stroke
738 Association. *Stroke*

739 Jiang-Xie LF, Drieu A, Bhasiin K, Quintero D, Smirnov I, Kipnis J. 2024. Neuronal dynamics direct cerebrospinal fluid
740 perfusion and brain clearance. *Nature* 627: 157-64

741 Kara P, Friedlander MJ. 1999. Arginine analogs modify signal detection by neurons in the visual cortex. *J Neurosci* 19:
742 5528-48

743 Karagiannis A, Gallopin T, David C, Battaglia D, Geoffroy H, et al. 2009. Classification of NPY-expressing neocortical
744 interneurons. *J Neurosci* 29: 3642-59

745 Kawaguchi Y, Kubota Y. 1997. GABAergic cell subtypes and their synaptic connections in rat frontal cortex. *Cereb*
746 *Cortex* 7: 476-86

747 Kedarasetti RT, Drew PJ, Costanzo F. 2022. Arterial vasodilation drives convective fluid flow in the brain: a poroelastic
748 model. *Fluids Barriers CNS* 19: 34

749 Kilduff TS, Cauli B, Gerashchenko D. 2011. Activation of cortical interneurons during sleep: an anatomical link to
750 homeostatic sleep regulation? *Trends Neurosci* 34: 10-9

751 Kjaerby C, Andersen M, Hauglund N, Untiet V, Dall C, et al. 2022. Memory-enhancing properties of sleep depend on
752 the oscillatory amplitude of norepinephrine. *Nat Neurosci* 25: 1059-70

753 Knot HJ, Nelson MT. 1998. Regulation of arterial diameter and wall [Ca2+] in cerebral arteries of rat by membrane
754 potential and intravascular pressure. *The Journal of Physiology* 508 (Pt 1: 199-209

755 Kramer RS, Pearlstein RD. 1979. Cerebral cortical microfluorometry at isosbestic wavelengths for correction of
756 vascular artifact. *Science* 205: 693-6

757 Krawchuk MB, Ruff CF, Yang X, Ross SE, Vazquez AL. 2020. Optogenetic assessment of VIP, PV, SOM and NOS
758 inhibitory neuron activity and cerebral blood flow regulation in mouse somato-sensory cortex. *J Cereb Blood*
759 *Flow Metab* 40: 1427-40

760 Kress BT, Iliff JJ, Xia M, Wang M, Wei HS, et al. 2014. Impairment of paravascular clearance pathways in the aging
761 brain. *Annals of Neurology* 76: 845-61

762 Kubota Y, Shigematsu N, Karube F, Sekigawa A, Kato S, et al. 2011. Selective coexpression of multiple chemical
763 markers defines discrete populations of neocortical GABAergic neurons. *Cereb Cortex* 21: 1803-17

764 Le Gac B, Tournissac M, Belzic E, Picaud S, Dusart I, et al. 2025. Elevated pyramidal cell firing orchestrates arteriolar
765 vasoconstriction through COX-2-derived prostaglandin E2 signaling. *eLife* 13

766 Lee L, Boorman L, Glendenning E, Christmas C, Sharp P, et al. 2020. Key Aspects of Neurovascular Control Mediated
767 by Specific Populations of Inhibitory Cortical Interneurons. *Cereb Cortex* 30: 2452-64

768 Li N, Chen S, Guo ZV, Chen H, Huo Y, et al. 2019. Spatiotemporal constraints on optogenetic inactivation in cortical
769 circuits. *Elife* 8

770 Ma Y, Shaik MA, Kim SH, Kozberg MG, Thibodeaux DN, et al. 2016a. Wide-field optical mapping of neural activity and
771 brain haemodynamics: considerations and novel approaches. *Philos Trans R Soc Lond B Biol Sci* 371

772 Ma Y, Shaik MA, Kozberg MG, Kim SH, Portes JP, et al. 2016b. Resting-state hemodynamics are spatiotemporally
773 coupled to synchronized and symmetric neural activity in excitatory neurons. *Proc Natl Acad Sci U S A* 113:
774 E8463-E71

775 Mantyh PW, Allen CJ, Ghilardi JR, Rogers SD, Mantyh CR, et al. 1995. Rapid endocytosis of a G protein-coupled
776 receptor: substance P evoked internalization of its receptor in the rat striatum in vivo. *Proc Natl Acad Sci U*
777 *S A* 92: 2622-6

778 Martin JL, Sloviter RS. 2001. Focal inhibitory interneuron loss and principal cell hyperexcitability in the rat
779 hippocampus after microinjection of a neurotoxic conjugate of saporin and a peptidase-resistant analog of
780 Substance P. *The Journal of Comparative Neurology* 436: 127-52

781 Mathis A, Mamidanna P, Cury KM, Abe T, Murthy VN, et al. 2018. DeepLabCut: markerless pose estimation of user-
782 defined body parts with deep learning. *Nat Neurosci* 21: 1281-89

783 Matrongolo MJ, Ang PS, Wu J, Jain A, Thackray JK, et al. 2023. Piezo1 agonist restores meningeal lymphatic vessels,
784 drainage, and brain-CSF perfusion in craniosynostosis and aged mice. *Journal of Clinical Investigation* 134

785 Matsumura S, Yamamoto K, Nakaya Y, O'Hashi K, Kaneko K, et al. 2021. Presynaptic NK1 Receptor Activation by
786 Substance P Suppresses EPSCs via Nitric Oxide Synthesis in the Rat Insular Cortex. *Neuroscience* 455: 151-
787 64

788 McKay LC, Feldman JL. 2008. Unilateral ablation of pre-Botzinger complex disrupts breathing during sleep but not
789 wakefulness. *Am J Respir Crit Care Med* 178: 89-95

790 Morairty SR, Dittrich L, Pasumarthi RK, Valladao D, Heiss JE, et al. 2013. A role for cortical nNOS/NK1 neurons in
791 coupling homeostatic sleep drive to EEG slow wave activity. *Proc Natl Acad Sci U S A* 110: 20272-7

792 Osorio-Forero A, Cardis R, Vantomme G, Guillaume-Gentil A, Katsioudi G, et al. 2021. Noradrenergic circuit control
793 of non-REM sleep substates. *Curr Biol* 31: 5009-23 e7

794 Paul A, Crow M, Raudales R, He M, Gillis J, Huang ZJ. 2017. Transcriptional Architecture of Synaptic Communication
795 Delineates GABAergic Neuron Identity. *Cell* 171: 522-39 e20

796 Penny GR, Afsharpour S, Kitai ST. 1986. Substance P-immunoreactive neurons in the neocortex of the rat: A subset
797 of the glutamic acid decarboxylase-immunoreactive neurons. *Neuroscience Letters* 65: 53-59

798 Perrenoud Q, Geoffroy H, Gauthier B, Rancillac A, Alfonsi F, et al. 2012. Characterization of Type I and Type II nNOS-
799 Expressing Interneurons in the Barrel Cortex of Mouse. *Front Neural Circuits* 6: 36

800 Pfeffer CK, Xue M, He M, Huang ZJ, Scanziani M. 2013. Inhibition of inhibition in visual cortex: the logic of connections
801 between molecularly distinct interneurons. *Nat Neurosci* 16: 1068-76

802 Phillips EA, Hasenstaub AR. 2016. Asymmetric effects of activating and inactivating cortical interneurons. *Elife* 5

803 Pleil KE, Rinker JA, Lowery-Gionta EG, Mazzone CM, McCall NM, et al. 2015. NPY signaling inhibits extended amygdala
804 CRF neurons to suppress binge alcohol drinking. *Nat Neurosci* 18: 545-52

805 Poplawsky AJ, Kim SG. 2014. Layer-dependent BOLD and CBV-weighted fMRI responses in the rat olfactory bulb.
806 *Neuroimage* 91: 237-51

807 Renden RB, Institoris A, Sharma K, Tran CHT. 2024. Modulatory effects of noradrenergic and serotonergic signaling
808 pathway on neurovascular coupling. *Commun Biol* 7: 287

809 Roth KA, Katz RJ. 1979. Stress, behavioral arousal, and open field activity--a reexamination of emotionality in the rat.
810 *Neurosci Biobehav Rev* 3: 247-63

811 Ruff CF, Juarez Anaya F, Dienel SJ, Rakymzhan A, Altamirano-Espinoza A, et al. 2024. Long-range inhibitory neurons
812 mediate cortical neurovascular coupling. *Cell Rep* 43: 113970

813 Sahara S, Yanagawa Y, O'Leary DD, Stevens CF. 2012. The fraction of cortical GABAergic neurons is constant from
814 near the start of cortical neurogenesis to adulthood. *J Neurosci* 32: 4755-61

815 Schaeffer S, Iadecola C. 2021. Revisiting the neurovascular unit. *Nat Neurosci* 24: 1198-209

816 Scherer-Singler U, Vincent SR, Kimura H, McGeer EG. 1983. Demonstration of a unique population of neurons with
817 NADPH-diaphorase histochemistry. *J Neurosci Methods* 9: 229-34

818 Schulz K, Sydekum E, Krueppel R, Engelbrecht CJ, Schlegel F, et al. 2012. Simultaneous BOLD fMRI and fiber-optic
819 calcium recording in rat neocortex. *Nature Methods* 9: 597-602

820 Scott BB, Thiberge SY, Guo C, Tervo DGR, Brody CD, et al. 2018. Imaging Cortical Dynamics in GCaMP Transgenic Rats
821 with a Head-Mounted Widefield Macroscope. *Neuron* 100: 1045-58 e5

822 Seeger G, Hartig W, Rossner S, Schliebs R, Bruckner G, et al. 1997. Electron microscopic evidence for microglial
823 phagocytic activity and cholinergic cell death after administration of the immunotoxin 192IgG-saporin in
824 rat. *Journal of neuroscience research* 48: 465-76

825 Seibenhener ML, Wooten MC. 2015. Use of the Open Field Maze to measure locomotor and anxiety-like behavior in
826 mice. *J Vis Exp*: e52434

827 Shih AY, Mateo C, Drew PJ, Tsai PS, Kleinfeld D. 2012. A Polished and Reinforced Thinned-skull Window for Long-
828 term Imaging of the Mouse Brain. *Journal of Visualized Experiments*

829 Sicher AR, Starnes WD, Griffith KR, Dao NC, Smith GC, et al. 2023. Adolescent binge drinking leads to long-lasting
830 changes in cortical microcircuits in mice. *Neuropharmacology* 234: 109561

831 Sirotin YB, Das A. 2009. Anticipatory haemodynamic signals in sensory cortex not predicted by local neuronal activity.
832 *Nature* 457: 475-9

833 Smith RJ, Anderson RI, Haun HL, Mulholland PJ, Griffin WC, 3rd, et al. 2020. Dynamic c-Fos changes in mouse brain
834 during acute and protracted withdrawal from chronic intermittent ethanol exposure and relapse drinking.
835 *Addict Biol* 25: e12804

836 Smith SL, Otis TS. 2003. Persistent changes in spontaneous firing of Purkinje neurons triggered by the nitric oxide
837 signaling cascade. *J Neurosci* 23: 367-72

838 Sohal VS, Zhang F, Yizhar O, Deisseroth K. 2009. Parvalbumin neurons and gamma rhythms enhance cortical circuit
839 performance. *Nature* 459: 698-702

840 Staiger JF, Petersen CCH. 2021. Neuronal Circuits in Barrel Cortex for Whisker Sensory Perception. *Physiol Rev* 101:
841 353-415

842 Stringer C, Pachitariu M, Steinmetz N, Reddy CB, Carandini M, Harris KD. 2019. Spontaneous behaviors drive
843 multidimensional, brainwide activity. *Science* 364: 255

844 Tomioka R, Okamoto K, Furuta T, Fujiyama F, Iwasato T, et al. 2005. Demonstration of long-range GABAergic
845 connections distributed throughout the mouse neocortex. *Eur J Neurosci* 21: 1587-600

846 Tomioka R, Rockland KS. 2007. Long-distance corticocortical GABAergic neurons in the adult monkey white and gray
847 matter. *J Comp Neurol* 505: 526-38

848 Tran CHT, Peringod G, Gordon GR. 2018. Astrocytes Integrate Behavioral State and Vascular Signals during Functional
849 Hyperemia. *Neuron* 100: 1133-48 e3

850 Tricoire L, Vitalis T. 2012. Neuronal nitric oxide synthase expressing neurons: a journey from birth to neuronal
851 circuits. *Front Neural Circuits* 6: 82

852 Tu W, Cramer SR, Zhang N. 2024. Disparity in temporal and spatial relationships between resting-state
853 electrophysiological and fMRI signals. *Elife* 13

854 Turner KL, Gheres KW, Drew PJ. 2023. Relating Pupil Diameter and Blinking to Cortical Activity and Hemodynamics
855 across Arousal States. *J Neurosci* 43: 949-64

856 Turner KL, Gheres KW, Proctor EA, Drew PJ. 2020. Neurovascular coupling and bilateral connectivity during NREM
857 and REM sleep. *Elife* 9

858 Turrigiano GG. 2008. The self-tuning neuron: synaptic scaling of excitatory synapses. *Cell* 135: 422-35

859 Uhlirova H, Kilic K, Tian P, Thunemann M, Desjardins M, et al. 2016. Cell type specificity of neurovascular coupling in
860 cerebral cortex. *Elife* 5

861 van Veluw SJ, Hou SS, Calvo-Rodriguez M, Arbel-Ornath M, Snyder AC, et al. 2020. Vasomotion as a Driving Force for
862 Paravascular Clearance in the Awake Mouse Brain. *Neuron* 105: 549-61 e5

863 Vanlandewijck M, He L, Mae MA, Andrae J, Ando K, et al. 2018. A molecular atlas of cell types and zonation in the
864 brain vasculature. *Nature* 554: 475-80

865 Vo TT, Im GH, Han K, Suh M, Drew PJ, Kim SG. 2023. Parvalbumin interneuron activity drives fast inhibition-induced
866 vasoconstriction followed by slow substance P-mediated vasodilation. *Proc Natl Acad Sci U S A* 120:
867 e2220777120

868 Vruwink M, Schmidt HH, Weinberg RJ, Burette A. 2001. Substance P and nitric oxide signaling in cerebral cortex:
869 anatomical evidence for reciprocal signaling between two classes of interneurons. *J Comp Neurol* 441: 288-
870 301

871 Wang H, Germanson TP, Guyenet PG. 2002. Depressor and tachypneic responses to chemical stimulation of the
872 ventral respiratory group are reduced by ablation of neurokinin-1 receptor-expressing neurons. *J Neurosci*
873 22: 3755-64

874 Wiley RG, Lappi DA. 1999. Targeting neurokinin-1 receptor-expressing neurons with [Sar9,Met(O2)11 substance P-
875 saporin. *Neurosci Lett* 277: 1-4

876 Williams RH, Black SW, Thomas AM, Piquet J, Cauli B, Kilduff TS. 2019. Excitation of Cortical nNOS/NK1R Neurons by
877 Hypocretin 1 is Independent of Sleep Homeostasis. *Cereb Cortex* 29: 1090-108

878 Williams RH, Vazquez-DeRose J, Thomas AM, Piquet J, Cauli B, Kilduff TS. 2018. Cortical nNOS/NK1 Receptor Neurons
879 are Regulated by Cholinergic Projections From the Basal Forebrain. *Cereb Cortex* 28: 1959-79

880 Winder AT, Echagarruga C, Zhang Q, Drew PJ. 2017. Weak correlations between hemodynamic signals and ongoing
881 neural activity during the resting state. *Nat Neurosci* 20: 1761-69

882 Wölfle SE, Chaston DJ, Goto K, Sandow SL, Edwards FR, Hill CE. 2011. Non-linear relationship between
883 hyperpolarisation and relaxation enables long distance propagation of vasodilatation. *The Journal of*
884 *physiology* 589: 2607-23

885 Wright PW, Brier LM, Bauer AQ, Baxter GA, Kraft AW, et al. 2017. Functional connectivity structure of cortical calcium
886 dynamics in anesthetized and awake mice. *PLoS One* 12: e0185759

887 Wu YT, Bennett HC, Chon U, Vanselow DJ, Zhang Q, et al. 2022. Quantitative relationship between cerebrovascular
888 network and neuronal cell types in mice. *Cell Rep* 39: 110978

889 Yan XX, Garey LJ. 1997. Morphological diversity of nitric oxide synthesising neurons in mammalian cerebral cortex. *J*
890 *Hirnforsch* 38: 165-72

891 Yan XX, Jen LS, Garey LJ. 1996. NADPH-diaphorase-positive neurons in primate cerebral cortex colocalize with GABA
892 and calcium-binding proteins. *Cereb Cortex* 6: 524-9

893 Zhang Q, Gheres KW, Drew PJ. 2021. Origins of 1/f-like tissue oxygenation fluctuations in the murine cortex. *PLoS*
894 *Biol* 19: e3001298

895 Zhang Q, Haselden WD, Charpak S, Drew PJ. 2023. Could respiration-driven blood oxygen changes modulate neural
896 activity? *Pflugers Arch* 475: 37-48

897 Zhang Q, Roche M, Gheres KW, Chaigneau E, Kedarasetti RT, et al. 2019. Cerebral oxygenation during locomotion is
898 modulated by respiration. *Nat Commun* 10: 5515

899 Zhang Q, Turner KL, Gheres KW, Hossain MS, Drew PJ. 2022. Behavioral and physiological monitoring for awake
900 neurovascular coupling experiments: a how-to guide. *Neurophotonics* 9: 021905

901 Zhao J, Manza P, Wiers C, Song H, Zhuang P, et al. 2020. Age-Related Decreases in Interhemispheric Resting-State
902 Functional Connectivity and Their Relationship With Executive Function. *Frontiers in Aging Neuroscience* 12

903 Zielinski MR, Atochin DN, McNally JM, McKenna JT, Huang PL, et al. 2019. Somatostatin+/nNOS+ neurons are
904 involved in delta electroencephalogram activity and cortical-dependent recognition memory. *Sleep* 42

905